Global 3-D distribution of aerosol composition by synergistic use of CALIOP and MODIS observations

Rei Kudo[1], Akiko Higurashi[2], Eiji Oikawa[1], Masahiro Fujikawa[3], Hiroshi Ishimoto[1], and Tomoaki Nishizawa[2]

5   [1]Meteorological Research Institute, Japan Meteorological Agency, Tsukuba, 305-0052, Japan
[2]National Institute for Environmental Studies, Tsukuba, 305-8506, Japan
[3]Research Institute for Applied Mechanics, Kyusyu University, Kasuga, 816-8580, Japan

Correspondence to: Rei Kudo (reikudo@mri-jma.go.jp)

Abstract. For the observation of the global three-dimensional distribution of aerosol composition and the evaluation of
10   shortwave direct radiative forcing (SDRF) by aerosols, we developed a retrieval algorithm that uses observation data of the
Cloud-Aerosol Lidar with Orthogonal Polarization (CALIOP) onboard the Cloud Aerosol Lidar Infrared Pathfinder Satellite
Observations (CALIPSO) satellite, and the Moderate Resolution Imaging Spectroradiometer (MODIS) onboard Aqua. The
CALIOP-MODIS retrieval optimizes the aerosol composition to both the CALIOP and MODIS observations in the daytime.
Aerosols were assumed to be composed of four aerosol components: water-soluble particles (WS), light-absorbing particles
15   (LA), dust (DS), and sea salt (SS). The outputs of the CALIOP-MODIS retrieval are the vertical profiles of the extinction
coefficient (EC), single-scattering albedo (SSA), and asymmetry factor (AF) of total aerosols, and the ECs of WS, LA, DS,
and SS. Daytime observations of CALIOP and MODIS in 2010 were analysed by the CALIOP-MODIS retrieval. The global
means of the aerosol optical depth (AOD) at 532 nm were 0.147 ± 0.148 for total aerosols (WS+LA+DS+SS), 0.072 ± 0.085
for WS, 0.027 ± 0.035 for LA, 0.025 ± 0.054 for DS, and 0.023 ± 0.020 for SS. AODs of the CALIOP-MODIS retrieval were
20   between those of the CALIPSO and MODIS standard products in 2010. The global means of SSA and AF were 0.940 ± 0.038
and 0.718 ± 0.037; these values are in the range of those reported by previous studies. The horizontal distribution of each
aerosol component was reasonable; for example, DS was large in desert regions, and LA was large in the major regions of
biomass-burning and anthropogenic aerosol emissions. The AOD, SSA, AF, and fine and coarse median radii of the CALIOP-
MODIS retrieval were compared with those of the AERONET products. AOD at 532 and 1064 nm of the CALIOP-MODIS
25   retrieval agreed well with the AERONET products. SSA, AF, and fine and coarse median radii of the CALIOP-MODIS
retrieval were not far from those of the AERONET products, but the variations were large, and the coefficients of determination
for linear regression between them were small. In the retrieval results for 2010, the clear sky SDRF values for aerosols at the
top and bottom of the atmosphere were -4.99 ± 3.42 and -13.10 ± 9.93 W m^{-2}, respectively, and the impact of aerosols on the
heating rate was from 0.0 to 0.5 K day^{-1}. These results are generally similar to those of previous studies, but the SDRF at the
30   bottom of the atmosphere is larger than that reported previously. Comparison with previous studies showed that the CALIOP-
MODIS retrieval results were reasonable with respect to aerosol composition, optical properties, and the SDRF.

1 Introduction

Aerosols have significant impacts on climate change through modification of the atmospheric radiation budget by scattering and absorbing solar radiation (aerosol-radiation interaction) and by modifying cloud physical properties (aerosol-cloud interaction). However, large uncertainties remain in evaluations of the aerosol impact on global warming (Arias et al., 2021) because of the large spatiotemporal variations in aerosol composition and the complex physical processes of aerosol-radiation and aerosol-cloud interactions. Because the radiative forcing of almost all aerosol chemical components is negative, aerosols contribute to the suppression of global warming; however, the radiative forcing of light-absorbing aerosols such as black carbon (BC) is positive (e.g., Matsui et al., 2018). Observations of spatiotemporal variations of aerosol composition are therefore essential for better understanding of the impacts of aerosols on climate change.

Several ground-based remote sensing methods to retrieve aerosol composition have been developed. Kudo et al. (2010a) estimated 10-year variations of water-soluble particles (WS), BC, dust (DS), and sea salt (SS) from the direct and diffuse solar radiation in the visible and near infrared wavelength regions measured by two pyranometers and two pyrheliometers. Nishizawa et al. (2007, 2008, 2011, 2017) retrieved concentrations of WS, BC, DS, and SS by using conventional Mie-scattering lidar as well as high-spectral-resolution lidar or Raman lidar data from the Asian Dust and Aerosol Lidar Observation Network (AD-Net; Sugimoto et al., 2015; Shimizu, et al., 2016). The Aerosol Robotics Network (AERONET; Holben et al., 1998) is an observational network of sun-sky radiometers that provides aerosol optical depth (AOD), single-scattering albedo (SSA), asymmetry factor (AF), phase function, and complex refractive index data products. Schuster et al. (2005) and Dey et al. (2006) inferred BC concentrations from the AERONET-retrieved size distribution and complex refractive index. They considered internal and external mixtures of BC, sulfate, organic carbon, DS, and water. Satellite remote sensing has also been used for estimating aerosol composition and investigating global distributions. For example, Higurashi and Nakajima (2002) and Kim et al. (2007) retrieved the spatiotemporal distributions of sulfate, carbonaceous, DS, and SS aerosols from spectral information on radiances observed by satellite imagers. The Cloud-Aerosol Lidar with Orthogonal Polarization (CALIOP) onboard the Cloud Aerosol Lidar Infrared Pathfinder Satellite Observations (CALIPSO) satellite has been utilized to classify aerosols at different altitudes (Winker et al., 2010). CALIOP Version 3 products classify seven aerosol types: clean marine, DS, polluted continental, clean continental, polluted DS, smoke, and stratospheric aerosols (Omar et al., 2009). In the CALIOP Version 4 product, tropospheric aerosols are subdivided into seven types, and stratospheric aerosols into four types (Kim et al., 2018). These ground- and satellite-based methods assume that aerosols consist of a few components with different sizes, light-absorbing features, and shapes (spherical or non-spherical), and they retrieve the aerosol composition from optical measurements made by using different wavelengths and polarization.

The above-mentioned remote sensing methods retrieve aerosol data obtained by a single instrument. Recently, synergistic remote sensing methods using active and passive sensors have been developed. Passive sensors such as spectral radiometers and polarimeters provide the columnar properties of aerosols, whereas aerosol vertical profiles are obtained by active sensing by lidar. The LIRIC (Chaikovsky et al., 2016) and GARRLiC (Lopatin et al., 2013) algorithms retrieve the

65   vertical profiles of aerosol physical and optical properties from lidar and AERONET sun-sky radiometer observations. SKYLIDAR (Kudo et al., 2016) estimates aerosol vertical profiles from both AD-Net lidar and SKYNET sky radiometer observations (Nakajima et al., 2020). Xu et al. (2021) have retrieved aerosol physical and optical properties and ocean parameters such as chlorophyll *a* concentration and surface wind speed from lidar and polarimetric observations over the ocean obtained during the ORACLES field campaign (Redemann et al., 2021).

70   To observe the global three-dimensional distribution of the aerosol composition, we have developed two aerosol composition retrieval methods that use the observations of CALIOP and the Moderate Resolution Imaging Spectroradiometer (MODIS) onboard the Aqua satellite. One is the CALIOP retrieval, which estimates the aerosol composition from the CALIOP observation in the day and night time. The other is the CALIOP-MODIS retrieval that optimizes the aerosol composition to both the CALIOP and MODIS observations in the daytime. In this study, we describe the CALIOP-MODIS retrieval. MODIS

75   uses multi-wavelength information to retrieve the columnar properties of aerosols, but it cannot obtain aerosol vertical profiles, and strong surface reflection (e.g., snow, desert) makes the retrieval difficult. CALIOP observations provide information on aerosol vertical profiles, but only limited wavelength information. The synergistic use of both instruments can compensate for the weak points of each. In this study, we assume aerosols to consist of four components with different sizes, light-absorbing features, particle mixtures, and shapes. We defined these components as WS, light-absorbing particles (LA), DS, and SS. The

80   global three-dimensional distributions of these components were estimated from the CALIOP-MODIS retrieval, and the aerosol shortwave direct radiative forcing (SDRF) of each component under clear sky conditions was investigated.

        This article is organized as follows. The CALIOP and MODIS observation data used for the retrievals are described in Sect. 2. The retrieval algorithms and the SDRF calculation method are described in Sect. 3. The uncertainties in the retrieval results are evaluated by using simulated CALIOP and MODIS observation data in Sect. 4. The global three-dimensional

85   distribution of aerosol compositions and the shortwave direct radiative forcing in 2010 are analysed in Sect. 5. All of the results are summarized in Sect. 6.

2 Data

2.1 Input of the CALIOP-MODIS retrievals

In this study, to retrieve the aerosol components, we made a match-up data set of CALIOP attenuated backscatter coefficients

90   (ABCs), MODIS radiances, surface albedo, and meteorological data acquired along the orbital track of A-train satellites, which includes the CALIPSO and Aqua satellites. The CALIOP data comprise the ABCs at 532 and 1064 nm and the depolarization ratio (DR) at 532 nm in the CALIPSO Lidar Level 1B Version 4 data product (Getzewich et al., 2018; Kar et al., 2018; Vaughan et al., 2019). The horizontal resolution of the original ABC data set is 333 m, and the vertical resolution is 30 m for the ABC at 532 nm, and 60 m for the ABC at 1064 nm. In this study, to reduce signal noise, we created a new data set with horizontal

95   and vertical resolutions of 1 km and 120 m, respectively, by calculating running means using horizontal and vertical windows of 10 km and 120 m, respectively. Clear sky (cloud-free) profiles in the CALIOP-MODIS retrieval, selected by using the

vertical feature mask (VFM) product of CALIPSO Lidar Level 2 Version 4 (Liu et al., 2019), were used. The VFM product describes layer classification information (clear air, cloud, tropospheric aerosol, stratospheric aerosol, surface, subsurface, etc.) observed by lidar and provides a cloud–aerosol discrimination (CAD) score, which is the confidence level for cloud/aerosol

100 classification. CAD can range from –100 to +100, where positive (negative) values indicate clouds (aerosols). A higher absolute value indicates greater confidence in the classification result. In this study, we used aerosol/cloud classification results with a CAD score greater than 70 for quality assurance (Liu et al., 2009).

We used MODIS Level 1B Calibrated Radiances (MYD02SSH, Collection 6.0) in bands 1 (620–670 nm) and 2 (841–876 nm) with along- and across-track resolutions of 5 km. To exclude cloud-contaminated observations, we used the Level 2

105 Cloud Mask Product (MYD35_L2, Collection 6.0; Ackerman et al., 2010). We used the black- and white-sky albedo of MCD43C3 Collection 6.0 (Schaaf et al., 2002; Wang et al., 2018) for the land surface reflection in the forward calculation of MODIS observations (Sect. 3.1.2.3). The clear sky radiances and albedos at the nearest pixel within a 10-km range from the near-nadir measurements (~3° off nadir) of CALIOP were selected for retrieval.

As ancillary data for the forward calculations of CALIOP and MODIS observations, we used pressure, temperature,

110 relative humidity, ozone concentration, and ocean surface wind speed from the MERRA-2 reanalysis data product (Gelaro et al., 2017). The ocean surface wind speed was used in calculating the ocean surface reflection in the forward model of the MODIS observations.

2.2 Data for comparison of retrieval results

The results of the CALIOP-MODIS retrievals in 2010 are compared with the CALIPSO and MODIS standard products and

115 AERONET products in Sect. 5. The CALIPSO standard product comprises the monthly means of AOD and the extinction coefficient (EC) in the cloud free daytime data set of the CALIPSO Lidar Level 3 Tropospheric Aerosol product Version 4 (Tackett et al., 2018), which has longitudinal, latitudinal, and vertical resolutions of 5°, 2°, and 60 m, respectively. The MODIS standard product comprises the monthly means of AOD in the MYD08_M3 Collection 6.1 Aqua Atmosphere Monthly Global Product (Platnick et al., 2015), with longitudinal and latitudinal resolutions of 1°. The annual means were calculated from the

120 monthly means. The AERONET products comprise AOD, SSA, AF, and fine and coarse mode radii in the level 2 data set of the version 3 inversion (Giles et al., 2019; Sinyuk et al., 2020).

3 Methods

3.1 Retrieval methods

3.1.1 Retrieval procedure

125 Figure 1 is a flow diagram of the retrieval procedures. The vertical profiles of the dry volume concentrations (DVCs) of WS, LA, DS, and SS, and the columnar values of the dry median radius values (DMRs) of the fine (WS and LA) and coarse modes

(DS) are optimized to all CALIOP and MODIS measurements. The DMR of SS is given by a parameterization that uses the ocean surface wind speed (Erickson and Duce, 1988). In this study, DVC and DMR are defined as the volume concentration and median radius, respectively, at a relative humidity of 0 %. Only the vertical layers discriminated as aerosols in the VFM

130 data are targeted for retrieval, and the CALIOP-MODIS retrieval is conducted for only clear sky data in the daytime. If clouds are detected in the VFM data, the CALIOP-MODIS retrieval is not conducted.

Inversion is conducted by the optimal estimation technique developed by Kudo et al. (2016). The state vector is optimized simultaneously to the measurements and a priori constraints by minimizing the following objective function:

$$f(x) = \left(y^{obs} - y(x)\right)^T (W^2)^{-1}\left(y^{obs} - y(x)\right) + y_a(x)^T (W_a^2)^{-1} y_a(x), \qquad (1)$$

135 where x is the state vector to be optimized, vector y^{obs} represents the CALIOP and MODIS measurements, vector $y(x)$ represents the calculations by the forward models corresponding to y^{obs}, W^2 is the covariance matrix of y, vector $y_a(x)$ gives the a priori constraints for x, and W_a^2 is an associated covariance matrix. The minimization of $f(x)$ is conducted by an iterative algorithm, with logarithmic transformation applied to x and y for stable and fast convergence of the iteration. Because the CALIOP measurements can have negative values caused by large signal noise, CALIOP measurements were transformed by

140 $Y = \ln(y - y_{min})$, where y_{min} is a possible minimum value of y. The best solution of x, which minimizes $f(x)$, is searched by the iteration of $x_{k+1} = x_k + \alpha d$, in $\ln(x)$ space, where vector d is determined by the Gauss-Newton method, and the scalar α is determined by a line search with the Armijo rule. The details of the forward models of aerosol physical and optical properties and of the CALIOP and MODIS observations are described in Sect. 3.1.2, and the details of the CALIOP-MODIS retrieval are described in the Sect. 3.1.3.

145 ### 3.1.2 Forward models

3.1.2.1 Forward model of aerosol physical and optical properties

We assumed that the aerosols consisted of four components: WS, LA, DS, and SS. Their physical and optical properties at relative humidities of 0 and 80 % are summarized in Table 1. WS and LA are small particles with small AF. DS and SS are large particles with large AF. LA and DS are light-absorbing particles and have small SSA. WS and SS have large SSA.

150 WS were assumed to be a mixture of sulfates, nitrates and organic and water-soluble substances (Hess et al., 1998). Their shape was assumed to be spherical, and their refractive index was defined from the OPAC database (Hess et al., 1998). We considered WS to grow hygroscopically and used the dependencies of particle size and refractive index on relative humidity given in the OPAC database.

We defined LA as an internal mixture of BC and WS, and introduced the core-grey shell (CGS) model (Kahnert et

155 al., 2013). CGS model has a spherical shape with a BC core and a shell consisting of a homogeneous mixture of WS and BC. The optical properties of CGS model are better representations of a realistic encapsulated aggregate model than the internally homogeneous mixture model obtained by using the Maxwell Garnett mixing rule (MG; Maxwell Garnett, 1904) and the core-shell (CS) model. The optical properties (EC, SSA, AF, and the lidar ratio [LR]) of CGS have values between those of the CS

and MG models (Table 1). Kahnert et al. (2013) defined a CGS model as a mixture of BC and sulfate, but we used WS instead
160   of sulfate in our definition. The details of the application of the CGS model are described in the Appendix. The refractive index
of BC was defined from the measurements of Chang and Charalampopoulos (1990). The hygroscopic growth of LA particles
was considered because the WS mixed in the shell are hydrophilic. We used the dependencies of the volume and refractive
index of WS on the relative humidity in the OPAC database for the shell of LA particles. In general, the volume fraction of
BC in an internally mixed particle changes spatiotemporally, but it is difficult to optimize the BC volume fraction in the
165   CALIOP-MODIS retrieval. Therefore, we fixed the BC volume fraction at 30 % of the total (BC+WS) volume, which is within
the range of values observed by the A-FORCE aircraft campaign in East Asia (Matsui et al., 2013). Because there are large
uncertainties in the particle models and the BC volume fraction, we conducted sensitivity tests using the different particle
models (CGS, CS, and MG) and BC volume fractions (15 and 30 %) (see Sect. 5).

The Voronoi particle model (Ishimoto et al., 2010) was used for DS in this study. Based on electron microscope
170   observations, the shape of the Voronoi particle model was created by a spatial Poisson-Voronoi tessellation. As an optional
model, the spheroid particle model of Dubovik et al. (2006) was also introduced in the retrieval. The linear depolarization ratio
(LDR) of a spheroid particle is less than that of a Voronoi particle (Table 1). We therefore conducted a sensitivity study of the
two particle models (see Sect. 5). The refractive index of DS was obtained from the database of Aoki et al. (2005); this database
was created from in situ measurements of dust samples in the Taklimakan Desert, China.

175   SS particles were assumed to be spherical, and the refractive index in the OPAC database was used. Hygroscopic
growth of SS was also considered, and the particle size and refractive index were changed depending on the relative humidity.
In retrievals over the ocean, four components (WS, LA, DS, and SS) were considered, but SS was ignored in retrievals over
land.

Each component was assumed to have a lognormal size distribution, and hygroscopic growth was considered by
180   including a growth factor as follows:

$$\frac{dV(r,RH)}{d\ln r} = \frac{V(RH)}{\sqrt{2\pi}\sigma}\exp\left[-\frac{1}{2}\left(\frac{\ln r-\ln r_m(RH)}{\sigma}\right)\right], \quad (2a)$$

$$r_m(RH) = GF(RH)r_{m,dry}, \quad (2b)$$

$$V(RH) = GF(RH)^3 V_{dry}, \quad (2c)$$

where r is radius, V is total volume, r_m is median radius, σ is the standard deviation, RH is relative humidity, GF is the growth
185   factor, $r_{m,dry}$ is the DMR, and V_{dry} is the DVC. The standard deviation is fixed at 0.45 for WS and LA, and at 0.8 for DS and
SS. These values are slightly larger than those of AERONET retrievals in worldwide locations (Dubovik et al., 2002). The
DMRs of fine (WS and LA) and coarse (DS) particles were parameters to be optimized. Here, the DMRs of WS and LA were
assumed to be the same. The DMR of SS was determined by the following relationship between the ocean surface wind speed
and the mass-mean radius for a relative humidity of 80 % (Erickson and Duce, 1988):

190          $$mmr = 0.422u + 2.12, \quad (3)$$

where mmr is the mass-mean radius and u is the ocean surface wind speed. The mass-mean radius is defined as the ratio of the fourth moment of the radius with respect to the number size distribution to the third moment (Lewis and Schwartz, 2004). The DMR was calculated from the mass-mean radius by using the lognormal size distribution obtained by Eq. (2). The growth factor GF for WS, the LA shell, and SS were obtained from the OPAC database.

Using the above-mentioned particle models and size distributions, we constructed data tables of EC, SSA, and the phase matrix for each model. The inputs of the data tables were the DVCs and DMRs of WS, LA, DS, and SS, and relative humidity. The outputs were the EC, SSA, the phase matrix, and the size distribution in the ambient relative humidity. Finally, the EC, SSA, phase matrix, AF, LR, LDR, and size distribution of total aerosols (WS+LA+DS+SS) were calculated according to the external mixture.

3.1.2.2 Forward model of CALIOP observations

We constructed a forward model to calculate the ABCs at 532 and 1064 nm and the DR at 532 nm from the vertical profiles of EC, LR, and LDR by the following lidar equations:

$$\beta_{co}(\lambda, z) = \left(\frac{\alpha_m(\lambda,z)}{S_m(\lambda,z)}\frac{1}{1+\delta_m(\lambda,z)} + \frac{\alpha_p(\lambda,z)}{S_p(\lambda,z)}\frac{1}{1+\delta_p(\lambda,z)}\right) \exp\left\{-2\int_{z'}^{TOA}\left(\alpha_m(\lambda,z') + \alpha_p(\lambda,z')\right)dz'\right\}, \quad (4)$$

$$\beta_{cr}(\lambda, z) = \left(\frac{\alpha_m(\lambda,z)}{S_m(\lambda,z)}\frac{\delta_m(\lambda,z)}{1+\delta_m(\lambda,z)} + \frac{\alpha_p(\lambda,z)}{S_p(\lambda,z)}\frac{\delta_p(\lambda,z)}{1+\delta_p(\lambda,z)}\right) \exp\left\{-2\int_{z'}^{TOA}\left(\alpha_m(\lambda,z') + \alpha_p(\lambda,z')\right)dz'\right\}, \quad (5)$$

$$\beta(\lambda, z) = \beta_{co}(\lambda, z) + \beta_{cr}(\lambda, z), \quad (6)$$

$$\delta(\lambda, z) = \beta_{cr}(\lambda, z)/\beta_{co}(\lambda, z), \quad (7)$$

where β and δ are the ABC and DR corresponding to the CALIOP observations; β_{co} and β_{cr} are co- and cross-polarization components of the ABC; λ is wavelength; z is altitude; $\alpha_{p/m}$, $S_{p/m}$, and $\delta_{p/m}$ are the EC, LR, and LDR, respectively, of particulate and molecular scattering; and TOA is the top of the atmosphere.

3.1.2.3 Forward model of MODIS observations

The band 1 and 2 radiances corresponding to the MODIS observations were calculated by the PSTAR vector radiative transfer model (Ota et al., 2010). The inputs of the forward model were the vertical profiles of the EC, SSA, and phase matrix calculated by the forward model of the aerosol optical properties. The surface reflection over the ocean was calculated from the surface wind speed by using the physical model of Nakajima and Tanaka (1983). The surface reflection over the land was assumed to be Lambert reflectance, and the actual albedo calculated from the black- and white-sky albedo of MODIS land surface products (Sect. 2.3) was used. The actual albedo from the black- and white-sky albedo was calculated by the method of Schaaf et al. (2002). Absorption of H_2, O_3, CO_2, O_2, O_3, and NO gases was considered in the radiative transfer calculation. The absorption coefficient was calculated by the correlated-k distribution method (Sekiguchi and Nakajima, 2008).

For rapid calculation, the response functions of bands 1 and 2 were divided to three sub-bands. The atmospheric vertical layers were assumed to consist of five vertical layers: 0–1 km, 1–3 km, 3–6 km, 6–10 km, and 10–120 km above the

surface. The influence of these assumptions was evaluated by referring to radiances simulated with the 10 sub-bands and 271 vertical layers. The properties of the aerosols, surfaces, and solar zenith angles used in the simulations were the same as those used in the simulations described in Sect. 4. The relative error of the radiances was less than 1 % for bands 1 and 2.

3.1.3 CALIOP-MODIS retrieval

225 The vertical profiles of the DVCs of WS, LA, DS, and SS, and the columnar values of the DMRs of fine (WS and LA) and coarse (DS) particles were optimized to all CALIOP and MODIS measurements. The DMR of SS was given by the parameterization using the ocean surface wind speed. The vertical profiles of the DMR were not considered in this study.

DS and SS are coarse particles, and they are more sensitive to the ABC at 1064 nm compared with the fine particles of WS and LA. Because only DS was assumed to be non-spherical, DVCs of DS and SS could be estimated from the ABC at

230 1064 nm and the DR at 532 nm. The DVCs of WS and LA could not be independently retrieved from only the ABC at 532 nm. Therefore, we introduced a priori constraints for WS and LA, as described later. The retrieval of the median radius from the satellite measurements is highly challenging, but Kaufman et al. (2003) have shown that the effective radius can be estimated from the wavelength dependencies of the ABC measurements at 532 and 1064 nm, and the radiance measurements at the near infrared wavelength. We conducted a similar sensitivity study to that conducted by Kaufman et al. (2003). The

235 scattering intensity is defined as,

$$I(\theta, \lambda) = P(\theta, \lambda)\tau_{sca}(\lambda)/(4\pi), \quad (8)$$

where θ is the scattering angle, λ is wavelength, P is the normalized phase function, and τ_{sca} is the scattering coefficient. In the calculations of the phase function and scattering coefficient, a lognormal size distribution with a standard deviation of 0.4 and the refractive index of DS were used. We calculated the scattering intensities for different wavelengths, scattering angles,

240 median radii, and particle shapes. Figure 2 shows the ratios of the scattering intensities. The scattering intensity at the scattering angle of 180° (Fig. 2a) represents lidar measurements, and the other angles (Fig. 2b, c, and d) represent MODIS measurements. For spherical and spheroidal particles, the scattering intensity ratios increase with an increase of the median radius within the ranges of 0.05–0.2 μm and 0.5–2.0 μm. The scattering intensity ratios for Voronoi particles increase with an increase of the radius over the entire radius range. These relationships indicate that the median radii of fine and coarse particles can be

245 estimated from the spectral information of CALIOP and MODIS measurements.

The CALIOP-MODIS retrieval procedure is diagrammed in Fig. 1, and the objective function is given by Eq. (1). The state vector $\boldsymbol{x}$ consists of the vertical profiles of DVCs of WS, LA, DS, and SS, and the DMRs of fine (WS and LA) and coarse (DS) particles. The DMRs of WS and LA were assumed to be same. The DMR of SS was given by the parameterization using ocean surface wind speed. The measurement vector $\boldsymbol{y}^{obs}$ was ABC at 532 and 1064 nm, DR at 532 nm, and the band 1

250 and 2 MODIS radiances. The forward calculation $\boldsymbol{y}(\boldsymbol{x})$ was processed by the forward models of the CALIOP (Sect. 3.1.2.2) and MODIS (Sect. 3.1.2.3) observations. The covariance matrix $\boldsymbol{W}^2$ was assumed to be diagonal, and the diagonal element of matrix $\boldsymbol{W}$ was obtained from the measurement accuracy. The measurement accuracy of ABC at 532 nm of CALIOP Version 3 was estimated by comparison with airborne high-spectral-resolution lidar (HSRL) data (Rogers et al., 2011). The mean

difference was 2.9 %, and the standard deviation was 20 % in the daytime. The bias of ABC at 532 nm of CALIOP Version 4

255 was smaller than that of CALIOP Version 3 (Getzewich et al. 2018), and our data set was smoothed by calculating the running mean (Sect. 2.1); thus, the accuracy of the ABC at 532 nm was assumed to be 15 %. The measurement accuracies of ABC at 1064 nm and DR at 532 nm were assumed to be 20 % and 50 %, respectively. Because we could not find previous reports of the measurement accuracies of ABC at 1064 nm and DR at 532 nm when we started this study, we used those values greater than the standard deviations for some scenes as the measurement accuracies. We defined the diagonal elements of $\boldsymbol{W}$ for the

260 band 1 and 2 radiances of MODIS by the following equation,

$$W = \begin{cases} 1.0, & \text{if } AOD \leq 0.05 \\ \exp(\alpha \ln(AOD) + \beta), & \text{if } 0.05 < AOD < 0.5, \\ 0.1, & \text{if } AOD \geq 0.5 \end{cases} \quad (9)$$

where the AOD value at 532 nm is obtained from the result of the CALIOP retrieval (Fujikawa et al., 2020), and the slope α and intercept β values were calculated from the equation $y = \exp(\alpha \ln(x) + \beta)$ and two ordered pairs of x and y: $(x, y) = (0.05, 1.0)$, and $(0.5, 0.1)$. We assumed that W for the radiances depended on the AOD, and that its range was from 0.1 to 1.0.

265 When the AOD is small, the upward radiance at the top of the atmosphere is significantly affected by the surface reflectance. However, we used the Lambert surface reflectance in the forward model of MODIS observations, and the surface albedo was obtained from the ancillary data. Therefore, when AOD was small, we decreased the relative contribution of the MODIS measurements to the objective function by W (Eq. (9)).

The retrieval of the vertical profiles of the DVCs is significantly affected by lidar signal noise. Smoothness of the

270 vertical profiles of the DVCs of WS, LA, DS, and SS was assumed, and an a priori smoothness constraint was introduced by using the second derivatives for the vertical profiles of the DVCs:

$$y_a(\boldsymbol{x}) = (\cdots \quad \ln v_{dry}(z_{i-1}) - 2\ln v_{dry}(z_i) + \ln v_{dry}(z_{i+1}) \quad \cdots), \quad (10)$$

where v_{dry} is the DVC at altitude z. The vertical variation of the DVCs was limited by minimizing Eq. (10). The covariance matrix $\boldsymbol{W}_a^2$ in Eq. (1) was assumed to be a diagonal matrix, and the values of the diagonal elements used for the smoothness

275 constraints were 0.2.

It is difficult to retrieve the DVCs of WS and LA independently from only the ABC at 532 nm. Therefore, we introduced two a priori constraints. First, the similarity of the vertical profiles of WS and LA was introduced. If the emission source of LA is the same as that of WS, for example, as with biomass-burning emissions, the vertical profile of LA would be similar to that of WS near the emission source. We assumed that the vertical profile shape of LA was similar to that of WS,

280 and the vertical profiles of LA and WS were constrained by

$$y_a(\boldsymbol{x}) = (\cdots \quad \ln[v_{dry,LA}(z_i)/v_{dry,LA}(z_{i+1})] - \ln[v_{dry,WS}(z_i)/v_{dry,WS}(z_{i+1})] \quad \cdots), \quad (11)$$

where $v_{dry,LA/WS}$ are the DVCs of LA and WS at altitude z_i. The vertical changes in the DVCs of WS and LA approach the same values when Eq. (11) is minimized. The second constraint was the inequality of the AODs of LA and WS. In the AERONET product at worldwide locations, SSA ranges from 0.8 to 1.0 (Dubovik et al., 2002), but the SSA of LA is less than

285 0.8 (Table 1). Thus, the AOD of WS is greater than that of LA. Therefore, we introduced the following log barrier function as a constraint:

$$y_a(\boldsymbol{x}) = -\ln\left(1 - \frac{\tau_{LA}(532nm)}{\tau_{WS}(532nm)}\right), \quad (12)$$

where $\tau_{LA/WS}(532nm)$ are the AODs of LA and WS at 532 nm. When the AOD of LA approaches the AOD of WS, Eq. (12) approaches infinity, and the objective function (Eq. (1)) also becomes infinity. The similarity and inequality constraints limited

290 the retrieval range of LA and prevented abnormal solutions. The diagonal elements of $\boldsymbol{W}_a$ were assumed to be 1.0 for both the similarity and inequality constraints.

In addition to the above-mentioned a priori constraints, we applied an a priori constraint to the DMR values of fine (WS and LA) and coarse (DS) particles. The spectral dependencies of the CALIOP and MODIS measurements have information on the particle radius. However, the large noise in the CALIOP measurements affects the spectral dependencies

295 of the CALIOP measurements, and errors in the given surface reflectance affect the forward calculation of the MODIS measurements. To avoid abnormal solutions, therefore, we constrained the DMR values by Eq. (13):

$$\boldsymbol{y}_a(\boldsymbol{x}) = r_{m,fine/coarse} - r_{m,fine/coarse}^{a\ priori}, \quad (13)$$

where r_m is the DMR of fine and coarse particles, and $r_m^{a\ priori}$ is the a priori value. We assumed that $r_m^{a\ priori}$ was 0.1 μm for fine particles and 2.0 μm for coarse particles. The diagonal elements $\boldsymbol{W}_a$ for the constraint of the DMR was assumed to be 0.2

300 for fine particles and 0.3 for coarse particles.

The minimization of the objective function was based on the Gauss-Newton method (Sect. 3.1.1). This method requires the numerical derivatives of $\boldsymbol{y}(\boldsymbol{x})$, where vector $\boldsymbol{x}$ consists of the vertical profiles of the four aerosol components and the fine/coarse median radii, and the number of the elements is on the order of from 10 to 100. The forward calculation of the MODIS observations by PSTAR is time consuming. For more rapid calculation, therefore, we approximated the numerical

305 derivatives of the radiances at bands 1 and 2 for the DVCs of WS, LA, DS, and SS. First, the numerical derivative was calculated from the monochromatic radiative transfer calculation at the centre wavelengths of bands 1 and 2. Because logarithmic transformation was applied to $\boldsymbol{x}$ and $\boldsymbol{y}(\boldsymbol{x})$, and the best solution of $\boldsymbol{x}$ was searched in $\log(\boldsymbol{x})$ space, the numerical derivative was defined as

$$\frac{\partial \log(y(x))}{\partial \log(x)} = \frac{\log(y(x+\Delta x)) - \log(y(x))}{\log(x+\Delta x) - \log(x)} = \frac{\log(y(x+\Delta x)/y(x))}{\log((x+\Delta x)/x)}. \quad (14)$$

310 $\frac{\partial \log(y(x))}{\partial \log(x)}$ is a relative value, and the radiances at bands 1 and 2 have no strong line absorptions. The monochromatic radiative transfer calculation for the numerical derivative is thus a good approximation. Second, the dependency of the numerical derivatives on DVC was investigated. Figure 3 shows an example of the approximated and reference numerical derivatives for the radiances at bands 1 and 2. The vertical profiles of WS, LA, DS, and SS used in the calculation of the numerical derivatives are shown in the first column of Fig. 3. The AOD at 532 nm used in the calculation was 0.3. The surface was the ocean, and

315 the wind speed was 15 m s^{-1}. The solar zenith angle was 40°. The reference numerical derivatives in the second column of Fig. 3 were calculated using the non-approximated forward model described in Sect. 3.1.2.3. The numerical derivatives mainly

depend on the DVCs (the third column of Fig. 3). The altitude dependency is shown in the fourth column of Fig. 3. The altitude dependency of LA, in particular, cannot be ignored. Using these relations, we approximated the numerical derivatives by the following procedure:

320 (1) For each aerosol component, 10th, 30th, and 80th percentiles of the DVCs are selected. When the number of aerosol layer is few, 25th and 75th percentiles of the DVCs are selected.

(2) The numerical derivatives for the selected DVCs are calculated for each aerosol component.

(3) The following equation is fit to the results of (2),

$$\frac{\partial \log(y(x))}{\partial \log(x)} = \begin{cases} (a_1 + a_2 z + a_3 z^2) v_{dry}, & \text{if three } v_{dry} \text{ are selected} \\ (a_1 + a_2 z) v_{dry}, & \text{if two } v_{dry} \text{ are selected} \end{cases}, \quad (15)$$

325 where v_{dry} is DVC and z is altitude. The coefficients, a_1, a_2, and a_3 are determined by the fitting.

(4) The numerical derivatives at all altitudes for each aerosol component are calculated by Eq. (15).

Figure 3 shows that the approximated numerical derivatives agree well with the reference values. However, the numerical derivatives of WS and SS near the surface have a unique behaviour (see the second and fourth columns of Fig. 3), and our method could not approximate these. At present, we are unable to determine the cause of this unique behaviour.

330 The objective function was minimized by the method described in Sect. 3.1.1 using the approximated numerical derivatives. The outputs of the CALIOP-MODIS retrieval were the vertical profiles of DVCs and ECs of WS, LA, DS, and SS, and the vertical profiles of EC, SSA, AF, as well as the size distribution of total aerosols at the ambient relative humidity. Even though we introduced some approximations for more rapid calculation, the CALIOP-MODIS retrieval is still time consuming. Therefore, the CALIOP-MODIS retrieval was conducted every 5 km along the track of the CALIPSO satellite's

335 orbit.

3.2 Clear sky shortwave direct radiative forcing

We prepared a module to calculate the aerosol optical properties (AOD, SSA, phase matrix) at any wavelengths in the solar wavelength region from the retrieved DVCs and DMRs of WS, LA, DS, and SS, and relative humidity by the forward model described in Sect. 3.1.2.1. The aerosol optical properties from 300 to 3000 nm were calculated by this module, and the clear

340 sky SDRF of aerosols was calculated by our developed radiative transfer model (Asano and Shiobara, 1989; Nishizawa et al., 2004; Kudo et al., 2011). The solar spectrum from 300 to 3000 nm was divided into 54 intervals. Gaseous absorption by H_2O, CO_2, O_2, and O_3 was calculated by the correlated-k distribution method. We calculated the SDRF of total aerosols (WS+LA+DS+SS) and of each component (WS, LA, DS, and SS) at the top of the atmosphere (TOA) and the bottom of the atmosphere (BOA) as follows:

345 $$SDRF = \Delta F^{TOA/BOA} = F_{with}^{TOA/BOA} - F_{without}^{TOA/BOA}, \quad (16)$$

where F_{with} is the net flux density with the aerosol (total or each component), and $F_{without}$ is the net flux density without the aerosol (total or each component). Furthermore, we calculated the impact of aerosols on the shortwave heating rate as,

$$\Delta T(z) = T_{with}(z) - T_{without}(z), \quad (17)$$

where T is the heating rate in units of K day^{-1}, and z is altitude.

4 Evaluation of retrieval uncertainties using simulation data

4.1 Configuration of the simulation

The uncertainties of the CALIOP-MODIS retrieval products were evaluated by using simulations of the CALIOP and MODIS observations. The simulations were conducted for 16 patterns of aerosol compositions (Table 2, Fig. 4) and for different AOD values, land and ocean surfaces, and different solar zenith angles. The transport of WS, LA, and DS in the free atmosphere was considered in the biomass-burning and dust cases (Table 2). The vertical profiles for the transported aerosols were assumed to have a normal distribution (Fig. 4). The boundary layer height was 2 km, and the EC of the aerosols in the boundary layer decreased linearly with increasing altitude (Fig. 4). DMRs of 0.07, 0.1, and 0.15 µm were used for WS and LA, and of 1.0, 2.0, and 4.0 µm for DS (Table 2). For AOD at 532 nm, values of 0.05, 0.1, 0.3, 0.5, 0.7, and 1.0 were used. Three land surface types were considered, and as surface albedo at bands 1 and 2, values of 0.05 and 0.50 for grass, 0.35 and 0.41 for desert, and 0.96 and 0.88 for snow, respectively, were used. These values were taken from the ECOSTRESS Spectral Library database (https://speclib.jpl.nasa.gov/ (last access: 27 August 2022). For the ocean surface, surface wind speeds of 5, 15, and 25 m s^{-1} were used. Solar zenith angles of 0°, 20°, 40°, and 60° were used. Random errors were added to the simulated CALIOP and MODIS observations and to the simulated surface albedo and surface wind speed data. The random errors for the CALIOP observations were less than ±15 % for ABC at 532 nm, ±20 % for ABC at 1064 nm, and ±50 % for DR at 532 nm. The random errors for the MODIS observations were less than ±5 % for the radiances at bands 1 and 2. The random error added to the surface albedo was less than ±0.10; this value is greater than the root mean square errors of the MOD43 albedo products: 0.07 for snow/ice surface (Stroeve et al., 2005, 2013; Williamson et al., 2016), 0.03 for agriculture, grassland, and forest (Wang et al., 2014). The random errors of surface wind speed over the ocean were considered to be less than ±5 m s^{-1}; this error is slightly larger than the root mean square errors obtained by comparing the reanalysis data with ship measurements: 2.7 to 4.10 m s^{-1} for the National Centers for Environmental Prediction-Department of Energy reanalysis, and from 1.67 to 2.77 m s^{-1} for the European Centre for Medium-Range Weather Forecasts Interim Re-Analysis (Li et al., 2013). Using the above conditions, the simulations of CALIOP and MODIS observations were conducted by the forward models described in Sects. 3.1.2.2 and 3.1.2.3. A total of 1152 simulations were conducted.

4.2 Uncertainties in the retrieval products

The retrievals of the columnar properties, AOD, SSA, and AF of total aerosols, AOD of WS, LA, DS, and SS, and DMRs of fine (WS and LA) and coarse (DS) particles are compared with the simulation results in Figure 5. Overall, the retrieval results are scattered near the one-to-one line. The AOD retrievals at 532 and 1064 nm are estimated particularly well. The AODs of

WS, DS, and SS also agree with the simulated values. However, the AOD of LA is overestimated, and the SSA at 532 nm is underestimated because of the overestimation of the AOD of LA. The AF of the CALIOP-MODIS retrieval agrees with the

380 simulated values. The DMRs of fine (WS and LA) and coarse (DS) particles agree well with the simulations. Figure 6 shows box-and-whisker plots of the differences between the retrievals and simulations for different values of the simulated AOD at 532 nm. All of the differences except for the AOD of LA and SSA decreased with an increase of the simulated AOD, particularly in the cases with AOD greater than 0.3. The SSA is underestimated over the entire range of simulated AOD, and the AOD of LA is overestimated. Table 3 summarizes the means and standard deviations of the differences between the

385 retrievals and simulations, separately for the land and ocean surface results. The retrieval results for the AOD of WS over the ocean are worse than those over the land because the retrieval of SS is added in the ocean surface cases. Both WS and SS are less light-absorbing particles; thus, they are not well distinguished in the retrieval. Moreover, random errors in the CALIOP and MODIS data and in the ocean surface wind data would also have affected the separation of WS and SS in the retrieval.

Figure 7 shows the relative differences in the EC for WS, LA, DS, and SS between the retrievals and simulations.

390 The relative differences in the EC for WS, LA, and DS are very large at altitudes from 3 to 5 km and from 6 to 7 km, because EC is very small near the bottom and top edges of the vertical distribution of transported aerosols (see Fig. 4). The relative difference in the EC for WS ranges from –0.3 to 0.1, and it tends to be underestimated at all altitudes except for the bottom and top edges of the transported aerosol layer. The median value of the relative differences is close to 0.0. The relative difference in the EC for LA tends to be overestimated and ranges from –1.0 to 2.0; The median value in the boundary layer is

395 close to 0.0, but the variances are large. The EC of DS tends to be underestimated; the relative difference ranges from –0.5 to 0.0. The relative difference in the EC for SS tends to be overestimated; the relative error is from –0.4 to 0.4. Table 4 shows the means and standard deviations of these relative differences and the differences for the EC, SSA, and AF of total aerosols. Similar to the results for the columnar properties, the results for the ECs of WS and SS over the ocean are worse than those over the land. The results for EC, SSA, and AF of total aerosols are also worse over the ocean.

400 Overall, the uncertainties in the retrieval results over the land are smaller than those over the ocean. The retrieval results become better in the larger AOD cases. The CALIOP-MODIS retrievals tend to overestimate the amount of LA, and SSA is underestimated. The retrieval of the DMR is a challenging problem, but the DMRs of fine (WS and LA) and coarse (DS) particles are estimated well.

5 Retrieval results from the CALIOP and MODIS observations in 2010

405 5.1 Global 3D distribution

The annual means of AOD and EC in the CALIOP-MODIS retrievals for 2010 are compared with the CALIPSO and MODIS standard products in Figure 8. The grid resolutions are 5° latitude by 2° longitude for the CALIOP-MODIS retrieval and the CALIOP standard product and 1° latitude by 1° longitude for the MODIS standard product. Note that the MODIS standard product is at 550 nm, but the difference of AOD between 532 and 550 nm is small. The horizontal distributions of AOD are

410   similar in all results. Large AOD values are distributed in the middle of the Atlantic Ocean, and in Africa and western, southern, and eastern Asia. The global mean ± standard deviation of AOD was 0.113 ± 0.161 for the CALIOP standard product, 0.147 ± 0.148 for the CALIOP-MODIS retrieval, and 0.164 ± 0.145 for the MODIS standard product. Thus, the global mean of the CALIOP-MODIS retrieval was between those of the CALIOP and MODIS standard products. Considering that the CALIOP-MODIS retrieval method used both CALIOP and MODIS observations, we consider the retrieval result to be reasonable. The

415   zonal means of EC in all results showed similar distributions. EC was large at latitudes from 60°S to 40°S and from 0° to 30°N. The top altitude of the vertical distribution was about 5 km at latitudes from 0° to 30°N. In the CALIOP-MODIS retrieval, an unnaturally large EC was observed at altitudes from 0 to 5 km and latitudes from 70°S to 80°S as well as at altitudes from 0 to 1 km and latitudes around 70°N. These unnaturally large values may be attributable to cloud contamination.

Figure 9 shows the horizontal distributions of SSA and AF. The global means of SSA and AF were about 0.940 ±

420   0.038 and 0.718 ± 0.037. Previous studies have shown that the global mean SSA is from 0.89 to 0.953 (Korras-Carraca et al., 2019; Kinne, 2019), and the global mean AF is 0.702 (Kinne, 2019). Our results are thus consistent with these previous studies. The SSA of the land was from 0.8 to 0.95 and was smaller than that of the ocean. The AF of the land was from 0.6 to 0.75 and also smaller than that of the ocean. These differences between land and ocean are due to the presence of SS over the ocean, because SSA and AF of SS are larger than those of the other aerosol components (Table 1).

425   Figure 10 depicts the horizontal distributions of the AOD of WS, LA, DS, and SS. The AOD of WS was large over Africa, western, southern, and eastern Asia, and the ocean. The large AOD of WS over the ocean might include a contribution from fine SS particles because a large AOD of WS was also seen over regions where the surface wind speed is large, such as the sea around Antarctica. A large AOD of LA was seen in central Africa, and southern and eastern Asia, which are major sources of aerosols from anthropogenic and biomass-burning sources. The AOD of DS was large around the desert regions of

430   northern Africa, and western, southern, and eastern Asia. Compared with those WS, LA, and DS, the AOD of SS was smaller and was uniformly distributed over the ocean. The global mean AOD was 0.072 ± 0.085 for WS, 0.027 ± 0.035 for LA, 0.025 ± 0.054 for DS, and 0.023 ± 0.020 for SS, respectively.

Figure 11 shows the zonal means of the EC of WS, LA, DS, and SS. Note that the range of EC depicted by colour bar in Fig. 11b is smaller than those in Figs. 11a, c, and d. The distribution of WS is almost the same as that of total aerosols

435   (Fig. 8b and d). The EC of WS was largest among the four aerosol components, and the EC of LA was smallest. The distribution of DS is concentrated between latitudes of 0° and 50°N, and the top altitude is about 5 km. SS is distributed across all latitudes, and its top altitude is about 1 km.

Figure 12 shows the DMRs of WS, LA, DS, and SS particles. The DMRs of WS, LA, and DS are large over the land and small over the ocean. This result indicates that particle size decreases away from the source regions. The DMR of SS is

440   the result of the parameterization using the ocean surface wind speed. Because the DMR of SS increases with an increase of wind speed, it is large in the midlatitudes, where cyclones caused by baroclinic instability occur frequently.

5.2 Comparisons with AERONET products

The CALIOP-MODIS retrieval results in 2010 were compared with the AERONET products. The CALIOP measurements are near-nadir (~3° off nadir) and include no swath observations. Most AERONET sites are far from the CALIPSO ground track.

445 Because mesoscale variability is a common feature of lower-tropospheric aerosols (Anderson et al., 2003), Omar et al. (2013) introduced as criteria for the coincidence a CALIPSO overpass with an AERONET site ±2 h and within a 40-km radius of the AERONET site. Schuster et al. (2012) used the coincidence criteria of ±30 min, within an 80-km radius, and a CALIOP digital elevation model surface elevation within 100 m of the AERONET site elevation. In this study, we used coincidence criteria of ±2 h, within a 40-km radius of an AERONET site, and within ±100 m of the AERONET site elevation. We thus compared the

450 means of CALIOP-MODIS retrievals satisfying these spatial criteria with the means of AERONET retrievals within ±2 h. A total of 91 samples met these criteria. The columnar properties of AOD at 532 and 1064 nm, SSA at 532 nm, AF at 532 nm, and the fine and coarse median radii of the volume size distribution at the ambient relative humidity were compared (Fig. 13). The AERONET optical properties at 532 and 1064 nm were calculated from the data at the AERONET wavelengths of 440, 500, 675, and 870 nm by linear interpolation and extrapolation in a log–log space. The fine and coarse median radii of the

455 CALIOP-MODIS retrieval data were calculated from the column-integrated volume size distribution by the same method as that used for AERONET data (Dubovik et al., 2002).

The AODs at 532 and 1064 nm of CALIOP-MODIS retrievals agreed well with those of AERONET; the slopes of the relationships were almost 1.0. The means and standard deviations of the relative differences between the CALIOP-MODIS retrievals and AERONET products were 0.04 ± 0.70 for AOD at 532 nm, and 0.14 ± 0.50 for AOD at 1064 nm.

460 SSA measurements were fewer than those of the other parameters. SSA retrieved from the sun-sky photometry has high uncertainty when AOD is small (Sinyuk et al. 2020; Kudo et al., 2021), and the AERONET Level 2 product does not provide the retrieved SSA when the AOD at 440 nm is less than 0.4. The coefficients of determination in the SSA comparison were small, and the CALIOP-MODIS retrievals were underestimated. The mean ± standard deviation of the absolute differences of SSA at 532 nm was -0.02 ± 0.04. The coefficients of determination for the AF comparison were also small, and

465 the CALIOP-MODIS retrievals were slightly underestimated. The mean ± standard deviation of the absolute differences of AF at 532 nm was -0.01 ± 0.04 for the CALIOP-MODIS retrieval. The coefficient of determination for the fine median radius of the CALIOP-MODIS retrieval was small, 0.015. However, the fine median radii of both the CALIOP-MODIS retrieval and the AERONET product lay in the same range from 0.1 to 0.2 μm, and the mean ± standard deviation of the absolute differences was 0.01 ± 0.04 μm. The comparison of the coarse median radius also showed a small coefficient of determination, 0.054.

470 However, the mean ± standard deviation of the absolute difference was small, 0.13 ± 0.60 μm, because the coarse median radii of the CALIOP-MODIS retrieval and the AERONET product lay in a similar range from 1.0 to 3.5 μm.

In summary, the AODs at 532 and 1064 of the CALIOP-MODIS retrievals showed good agreement with those of the AERONET products. SSA, AF, and fine and coarse median radii were not retrieved well, but their values were not far from those of the AERONET products. The vertical profile of EC was not compared with ground-based measurements in this study.

475 In the future, we will compare the vertical profile of EC with HSRL and Raman lidar measurements in the AD-Net (Nishizawa et al., 2017; Jin et al., 2022).

5.3 Influences of particle models

The assumed particle model is important in the retrieval of aerosols. We therefore investigated how different particle models influenced the retrievals by comparing the results when the spheroid particle model for DS was used in the retrievals instead
480 of the Voronoi particle model. Figures 14 and 15 show the differences of the retrieval results between the spheroid and Voronoi particle models. The AOD of DS for the retrieval with the spheroid model was greater than that for the retrieval with the Voronoi model (Fig. 14). Because the LDR of the spheroid particle model is smaller than that of the Voronoi model (Table 1), a large amount of DS was required to fit the DR calculated by the forward model to the DR measurements when the spheroid model was used. The AOD of WS and LA was decreased to compensate for the increase in the AOD of DS. The retrieved
485 DMR of DS was decreased (Fig. 15) by as much as about 0.6 μm in the heavy dust regions of Africa and western Asia. In Sect. 3.1.3, we showed that the median radius can be estimated from the spectral information of the scattering intensity. The scattering intensity ratio for spheroid particles changes from 0.8 to 3.0 in the range of the median radius from 1.0 to 5.0 μm, whereas the ratio of the scattering intensity for Voronoi particles changes from 0.8 to 2.6 in the median radius range from 1.0 to 5.0 μm (Fig. 2a). Since the scattering intensity ratio for spheroid particles is larger than that for Voronoi particles in the
490 median range from 1.0 to 5.0 μ m, the retrieved DMR of DS in the retrieval with the spheroid particle model was smaller than that in the retrieval with the Voronoi model. The DMRs of WS and LA were not influenced by the particle model used for DS.

The fixed volume fraction of BC is one of the assumptions associated with large uncertainties in this study. We therefore conducted the retrieval using LA with a BC volume fraction of 15 % instead of 30 %. Figure 16 shows the difference in the retrieval results between BC volume fractions of 15 % and 30 %. The AODs of WS and LA were slightly decreased
495 (Fig. 16b and c). The decrease in the global mean AODs was less than 0.01, but the decrease was large, up to 0.03, in Africa and western, southern, and eastern Asia. These results can be explained by the changes in SSA and LR. The SSA of LA with a BC fraction of 15 % is greater than that with a BC fraction of 30 %, and the LR of LA with a BC fraction of 15 % is smaller than that with a BC fraction of 30 % (Table 1). Larger SSA and smaller LR induces an increase in the values of the MODIS radiances and the CALIOP backscatter coefficients calculated by the forward models. As a result, smaller AOD and EC are
500 retrieved. The influence of the BC volume fraction on the retrieved AODs of DS and SS (Fig. 16d and e) and on the DMRs of the fine (WS and LA) and coarse (DS) particles was negligible (Table 5).

We also investigated the differences in retrievals when the CGS, CS, and MG models were used. The impacts on the retrieved AODs are summarized in Table 5. The retrieval using MG slightly increased the AOD of LA because of a slightly large LR (Table 1). Conversely, the retrieval using CS decreased the AOD of LA because the LR of CS was smaller than that
505 of CGS (Table 1). Different mixture models affected only the WS and LA retrievals, and the impact on the global mean AOD was less than 0.01.

5.4 Clear sky shortwave direct radiative forcing

The clear sky SDRF values of aerosols at the bottom and top of the atmosphere and the impacts of aerosols on the atmospheric heating rate were calculated from the retrieval results described in Sect. 5.1. The annual mean of the SDRF at the top of the

510 atmosphere was -4.99 ± 3.42 W m^{-2} (Fig. 17). Korras-Carraca et al. (2019) summarized the SDRF obtained by previous studies based on CALIOP and MODIS observations and chemical transport models. Previously obtained SDRF values ranged from -2.6 to -7.3 W m^{-2} for AODs from 0.074 to 0.18, and for SSAs from 0.89 to 0.97. Our results thus are in the range of previously obtained values. The horizontal distribution of the SDRF was also similar to those of previous studies (Korras-Carraca et al., 2019), and positive forcing was observed over desert and snow/ice surfaces with a large surface albedo. An advantage of this

515 study is that the SDRF of each aerosol component was determined. The global mean SDRF of WS was -2.99 ± 1.49 W m^{-2}, whereas the global mean SDRF of LA was 0.22 ± 0.94 W m^{-2}, and the SDRF of LA was positive in almost all regions. The global mean SDRF of DS was -0.93 ± 1.32 W m^{-2}, but the SDRF of DS was positive over desert and snow/ice surfaces. The SDRF of SS was negative worldwide at -0.96 ± 0.62 W m^{-2}.

The SDRF at the bottom of the atmosphere was negative in all regions, and the global mean was -13.10 ± 9.93 W

520 m^{-2} (Fig. 18). Previously reported values ranged from -10.7 to -6.64 W m^{-2} (Korras-Carraca et al., 2019). The CALIOP-MODIS retrieval result was more negative than the previous study results, but we could not determine the cause in this study. Further studies regarding to the differences of the aerosol optical properties and the configuration of the radiative transfer models are required but are beyond the scope of this study. Although the AOD of LA was smaller than the AOD of WS (Fig. 10), the SDRF of LA was largest. Furthermore, whereas the AOD of DS was comparable to that of SS, the SDRF of DS was

525 larger than that of SS. The small SSA of LA and DS decreases the diffuse irradiance reaching the surface, with the result that the SDRF at the bottom of the atmosphere becomes large (Kudo et al., 2010b).

Figure 19 shows the zonal means of the aerosol impacts on the heating rate. The vertical distribution of the impacts of the total aerosols corresponds to the distribution of the EC (Fig. 8). The maximum heating rate was about 0.5 K day^{-1}. Korras-Carraca et al. (2019) also found that the aerosol impact on the heating rate was large in the boundary layer, with a

530 maximum value of about 0.5 K day^{-1}. LA had the largest impact on the heating rate because of its small SSA, despite its small EC (Fig. 11). The values at all altitudes from 70°S to 80°S were unnatural for all aerosol components except SS. These unnatural values correspond to the unnatural ECs described in Sect. 5.1. Cloud contamination is a possible cause.

To summarize, the SDRF values calculated from the CALIOP-MODIS retrievals are consistent with those of previous studies. However, SDRF values at the bottom of the atmosphere were larger than in the previous studies. LA had a significant

535 impact on the SDRF at the top and bottom of the atmosphere and on the heating rate. The CALIOP-MODIS retrievals tended to overestimate the amount of LA. Thus, the retrieval of LA needs to be improved in the future.

6 Summary and conclusions

We developed the CALIOP-MODIS retrieval method for the observation of the global three-dimensional distribution of aerosol composition. The CALIOP-MODIS retrieval optimizes the aerosol composition to both CALIOP and MODIS observations in the daytime. In this study, aerosols were assumed to consist of four components, WS, LA, DS, and SS. The CALIOP-MODIS retrievals optimize the vertical profiles of the DVCs of the four components to the CALIOP and MODIS observations. Furthermore, the DMRs of fine (WS and LA) and coarse (DS) particles are optimized. The outputs of the CALIOP-MODIS retrievals are the vertical profiles of the EC, SSA, and AF of total aerosols (WS+LA+DS+SS) as well as the EC of WS, LA, DS, and SS, and their columnar integrated or mean values.

The uncertainties in the retrieval products were evaluated by using simulated data of the CALIOP and MODIS observations. Simulations were conducted for 16 aerosol vertical profile patterns by assuming the actual scenes in the daytime, including transport of dust, biomass-burning, and polluted dust with different AODs for total aerosols, different land (grass, desert, and snow) and ocean (different values of surface wind speed) surfaces, and different solar zenith angles. Random errors were also added to the CALIOP and MODIS observations, surface albedo, and surface wind speed. Overall, the performance of the CALIOP-MODIS retrievals was good. The retrieval results in the case of land surfaces were better than those for the ocean surface, because three components, excluding SS, were retrieved over the land surface, whereas four components were retrieved over the ocean surface. The retrieval results became better when the AOD was increased. When the AOD at 532 nm was greater than 0.3, the means and standard deviations of the relative differences between the CALIOP-MODIS retrievals and the simulations were –0.03 ± 0.11 for total AOD at 532 nm, –0.04 ± 0.12 for AOD of WS, 0.24 ± 0.99 for AOD of LA, and 0.05 ± 1.53 for AOD of DS in the land surface cases, and 0.10 ± 0.13 for total AOD at 532 nm, 0.05 ± 0.23 for AOD of WS, 0.78 ± 0.85 for AOD of LA, –0.09 ± 0.08 for AOD of DS, and –0.02 ± 0.30 for AOD of SS in the ocean surface case. The amount of LA tended to be overestimated; hence, SSA tended to be underestimated.

Daytime observation data of CALIOP and MODIS in 2010 were analysed by the CALIOP-MODIS retrievals. The global means of the AOD of total aerosols, WS, LA, DS, and SS were 0.147± 0.148, 0.072 ± 0.085, 0.027 ± 0.035, 0.025 ± 0.054, and 0.023 ± 0.020, respectively. Comparison with the CALIPSO and MODIS standard products showed that the total AOD of the CALIOP-MODIS retrieval was between those of the CALIPSO and MODIS standard products. Considering that the CALIOP-MODIS retrieval was a combined method using both CALIOP and MODIS observations, we believe that the results obtained are reasonable. The horizontal distribution of total AOD in the CALIOP-MODIS retrieval was similar to the distributions in the CALIPSO and MODIS standard products. The vertical distribution of the CALIOP-MOIDS retrieval was also similar to that in the CALIPSO standard product. However, an unnaturally large EC due to cloud contamination was found in both polar regions in the CALIOP-MODIS retrievals. Further study to improve cloud discrimination is required in the future.

Using the retrieval results for 2010, the AOD, SSA, AF, and fine and coarse median radii of the CALIOP-MODIS retrievals were compared with the corresponding AERONET products. The AODs at 532 and 1064 nm of the CALIOP-MODIS retrieval agreed well with the AERONET product. The relative difference of the CALIOP-MODIS retrieval was 0.04 ± 0.70

570 for AOD at 532 nm, and 0.14 ± 0.50 for AOD at 1064 nm. SSA, AF, and fine and coarse median radii of the CALIOP-MODIS retrievals were not far from those of the AERONET products, but the coefficients of determination for linear regressions between the CALIOP-MODIS retrievals and the AERONET products were small. The absolute difference between the CALIOP-MODIS retrieval and the AERONET product was –0.02 ± 0.04 for SSA, –0.01 ± 0.04 for AF, 0.01 ± 0.04 μm for the fine median radius, and 0.13 ± 0.60 μm for the coarse median radius.

575 The assumed particle model used in the retrieval causes large uncertainties. The influences of the DS and LA particle models on the retrievals were investigated. The dust model we used affected the retrievals of DS, WS, and LA. When the spheroid model was used instead of the Voronoi model, the AOD of DS was increased by about 0.015 ± 0.036, and the AODs of WS and LA were decreased by about 0.004 ± 0.012. These changes were consistent with the differences in LR and LDR between the spheroid and Voronoi models. The influence of the BC volume fraction on LA was also investigated. The

580 difference in AODs of WS and LA between retrievals using BC fractions of 15 and 30 % was about −0.005 ± 0.009 for the global mean. The influence of the internal mixture model used for LA was also investigated. Compared with the retrievals using the CGS model for LA, the retrieval using MG model increased the global mean AOD of WS and LA by about 0.002 ± 0.006, and the retrieval using the CS model decreased the AOD of WS and LA by 0.007 ± 0.011. These changes are consistent with the differences of SSA and LR among the MG, CS, and CGS models. The dust shape of the particle models had the largest

585 impact.

The clear sky SDRF of aerosols at the top and bottom of the atmosphere and the impact of aerosols on the heating rate was investigated using the retrievals for 2010. The SDRF values at the TOA and BOA were –4.99 ± 3.42 and –13.10 ± 9.93 W m^{-2}, respectively. The SDRF at TOA is in the range of previously reported values (from –2.6 to –7.3 W m^{-2}). However, the SDRF at BOA was larger than previously reported values (from –10.7 to –6.64 W m^{-2}). The aerosol impact on the heating

590 rate ranged from 0.0 to 0.5 K day^{-1}, consistent with previously reported values. The horizontal distributions of the SDRF at TOA and BOA, and the vertical distributions of the aerosol impacts on the heating rate were consistent with those of previous studies. An advantage of this study was that the SDRF was estimated for each aerosol component. The AOD of WS was largest among the four aerosol components: the SDRF of WS at TOA and BOA was large, but the impact of WS on the heating rate was small because WS is a less light-absorbing particle. In contrast, the AOD of LA was small, but its SDRF at TOA was

595 positive in most of the world, and its SDRF at BOA and its impact on the heating rate were largest among the four aerosol components. Thus, although the amount of LA was small, but the impact on the SDRF was significantly important.

Consequently, the AOD and EC of the CALIOP-MODIS retrieval in 2010 showed reasonable results when compared with the CALIPSO and MODIS standard products and the AERONET products. Furthermore, the SDRF values calculated from the CALIOP-MODIS retrievals were consistent with those of previous studies. However, there were some issues with

600 the CALIOP-MODIS retrievals. The AOD of LA tended to be overestimated, and the SSA was underestimated. Because the LA has a large impact on the SDRF, the overestimation of LA should be improved in a future study. The unnaturally large EC in both polar regions is also an important issue. The cloud discrimination should be improved. In this study, the vertical profile

of EC was not validated. We will compare the vertical profile of EC with the ground-based measurements by HSRL and Raman lidar of the AD-Net in the future.

605   The Earth Clouds, Aerosol and Radiation Explorer (EarthCARE) satellite is a joint mission of the European Space Agency and the Japanese Aerospace Exploration Agency (Illingworth et al., 2015). The atmospheric lidar (ATLID) onboard EarthCARE is a linearly polarized HSRL transmitting a spectrally narrow laser beam at 355 nm. The multispectral imager (MSI) onboard EarthCARE is an imager with seven bands from visible to infrared wavelengths. We are developing the application of the CALIOP-MODIS retrievals to the ATLID and MSI observations. We plan to investigate long-term changes

610   in the aerosol composition by using the CALIOP and MODIS observations together with ATLID and MSI observations. The results will contribute to our understanding of climate changes due to aerosols.

Appendix: Optimization of the core-grey shell model

BC has a complex morphology and forms mixtures with weakly light-absorbing particles. Previous studies have developed various simplified models, such as externally mixed homogeneous spheres, an internally mixed homogeneous sphere, and the

615   CS model. Comparison with realistic encapsulated aggregate models has shown that the externally mixed homogeneous spheres and the CS model underestimate the absorption cross section, and that the internally mixed homogeneous sphere overestimates the absorption cross section (Kahnert et al., 2012). The CGS model, developed by Kahnert et al. (2013), has a CS geometry, but compared with the original CS model with the same volume of BC and weakly light-absorbing particles, the volume fraction of the BC core to the total BC volume in a particle (f_{core}) is smaller than one in the CGS model, and the

620   remaining BC ($1 - f_{\mathrm{core}}$) is homogeneously mixed with weakly light-absorbing particles in the shell. The Maxwell Garnett mixing rule is used for the homogeneous mixing in the shell. The optical properties of the CGS model are better representations of a realistic encapsulated aggregate model than the externally mixed homogeneous spheres, internally mixed homogeneous sphere, and the CS model.

Kahnert et al. (2013) considered that the CGS model consists of BC and sulfate, and the value of f_{core} was optimized

625   to the optical properties of a realistic encapsulated aggregate model. However, we assumed that LA is a mixture of BC and WS, instead of BC and sulfate. WS is defined as a mixture of sulfates, nitrates, organic, water-soluble substances (Hess et al., 1998), and the SSA of WS is smaller than that of pure sulfate. The optimized values of f_{core} in Kahnert et al. (2013) cannot be applied in this study. Therefore, we optimized f_{core} to the optical properties of the Voronoi aggregate model with BC and WS (Ishimoto et al., 2019). The core of the model is a BC aggregate with a polyhedral Voronoi structure, and the adhering WS

630   shell is created by a simple model of surface tension derived from the artificial surface potential. The refractive index of the BC was obtained from the measurements of Chang and Charalampopoulos (1990). The refractive index of WS depends on the relative humidity and was obtained from the OPAC database (Hess et al., 1998). The optical properties of the Voronoi aggregate model were computed by the finite-difference time-domain method (Ishimoto et al., 2012) and discrete-dipole approximation (DDSCAT version 7.3; https://code.google.com/archive/p/ddscat/ (last access 25 December 2018); Draine and

635 Flatau, 1994). The database of optical properties of the Voronoi aggregate model was created under the following conditions. The volume ratio of shell to core (VR) was 0.0, 2.0, 5.0, 10.0, and 20.0. The volume-equivalent sphere radius was 10 sizes for each VR, and the radius range was from 0.02 to 0.2 µm for VR = 0.0, and from 0.06 to 0.6 µm for VR = 20.0. The relative humidity was 0, 50, 90, and 98 %. The wavelength was 340, 355, 380, 400, 500, 532, 675, 870, 1020, and 1064 nm. These are typical wavelengths of lidar and sky radiometer (Nakajima et al. 2020) measurements. The value of f_{core} was optimized to the

640 optical properties of the Voronoi aggregate model by the following procedure:

(1) f_{core} was changed from 0 to 1 with a step of 0.1.

(2) Optical properties (absorption cross section, SSA, and AF) of the CGS model with different values of f_{core} were calculated.

(3) The following objective function was calculated from the optical properties of the CGS and Voronoi aggregate models:

$$\chi(f_{core}) = \sum_{i=1}^{10} \sum_{j=1}^{4} \sum_{k=1}^{5} \left| \frac{\sigma_{abs}^{CGS}(f_{core},RH_j,VR_k) - \sigma_{abs}^{Voronoi}(r_i,RH_j,VR_k)}{\sigma_{abs}^{Voronoi}(r_i,RH_j,V_k)} \right| + \left| \frac{\omega_0^{CGS}(f_{core},r_i,RH_j,V_k) - \omega_0^{Voronoi}(r_i,RH_j,VR_k)}{\sigma\omega_0^{Voronoi}(r_i,RH_j,V_k)} \right| + $$

$$\left| \frac{g^{CGS}(f_{core},r_i,RH_j,VR_k) - g^{Voronoi}(r_i,RH_j,VR_k)}{g^{Voronoi}(r_i,RH_j,V_k)} \right|, \quad (A1)$$

where CGS/Voronoi indicate the CGS and Voronoi aggregate models, σ_{abs} is the absorption cross section; ω_0 is SSA; g is AF; r is the volume-equivalent sphere radius; RH is relative humidity; and VR is the volume ratio of shell to core. The objective function was calculated for each wavelength and for two particle size ranges, $r < 0.1$ µm and $r \geq 0.1$ µm.

650 Table A1 shows the objective functions for different values of f_{core}. The values of $f_{core} = 0$ and = 1 correspond to an internally mixed homogeneous sphere and the CS model, respectively. For $r < 0.1$ µm, the optimized values of f_{core} were 0.8 or 0.9, and the optimized CGS was close to CS. This result is caused by the fact that there are few monomers composing the Voronoi aggregate model when the particle radius is small, and the geometry of the Voronoi aggregate model is close to CS. For $r \geq 0.1$ µm, the f_{core} results were from 0.5 to 0.9. The optimized CGS approached that for internally mixed homogeneous spheres

655 as the wavelength increased. The same wavelength dependency was seen in the results of Kahnert et al. (2013). The optimized f_{core} in Table A1 was used for the calculation of the optical properties of the CGS.

Code availability.

The codes of the CALIOP-MODIS retrievals are available on request by contacting the first author of the paper. The software program is coded in Fortran and is compiled by Intel Fortran.

660 **Data availability.**

The retrieval results of the CALIOP-MODIS retrievals are available on request by contacting the first author of the paper.

Author contributions.

RK developed the codes of the CALIOP-MODIS retrievals and performed the numerical experiments, and the analysis of the
665 retrieval results. AH, EO, and MF processed the CALIOP and MODIS measurements and ancillary data before the retrievals.
HI developed the databases of the Voronoi particle models. TN planed the synergistic remote sensing by CALIOP and MODIS
and managed this project. RK prepared the paper with contributions from all co-authors.

Competing interests.

The authors declare that they have no conflict of interest.

670 **Acknowledgments.**

We gratefully acknowledge the uses of PSTAR of the OpenCLASTR (https://ccsr.aori.u-tokyo.ac.jp/~clastr/) and GRASP
spheroid-package (https://www.grasp-open.com). We thank the teams involved with CALIPSO, MODIS, and MERRA-2 for
their efforts in providing their products. We also thank the AERONET principal investigators and their staff for establishing
and maintaining AERONET at the 51 sites used in this investigation.

675 **Financial support.**

This research has been supported by the Japan Society for the Promotion of Science KAKENHI (grant no. 15H02808).

References

Ackerman, S. A., Frey, R., Strabala, K., Liu, Y., Gumley, L., Baum, B., and Menzel, P.: MODIS Atmosphere L2 Cloud Mask
Product. NASA MODIS Adaptive Processing System, Goddard Space Flight Center, USA,
680 http://dx.doi.org/10.5067/MODIS/MOD35_L2.006, 2015

Anderson, T. L., Charlson, R. J., Winker, D. M., Ogren, J. A., and Holmén, K.: Mesoscale variations of tropospheric aerosols,
J. Atmos. Sci., 60, 119-136, https://doi.org/10.1175/1520-0469(2003)060<0119:MVOTA>2.0.CO;2, 2003.

Aoki, T., Tanaka, T. Y., Uchiyama, A., Chiba, M., Mikami, M, Yabuki, S., Key, J. R.: Sensitivity experiments of direct
radiative forcing caused by mineral dust simulated with a chemical transport model, J. Meteor. Soc. Jpn., 83A, 315-331,
685 https://doi.org/10.2151/jmsj.83A.315, 2005.

Arias, P.A., Bellouin, N., Coppola, E., Jones, R.G., Krinner, G., Marotzke, J., Naik, V., Palmer, M.D., Plattner, G.-K., Rogelj, J., Rojas, M., Sillmann, J., Storelvmo, T., Thorne, P.W., Trewin, B., Achuta Rao, K., Adhikary, B., Allan, R.P., Armour, K., Bala, G., Barimalala, R., Berger, S., Canadell, J.G., Cassou, C., Cherchi, A., Collins, W., Collins, W.D., Connors, S.L., Corti, S., Cruz, F., Dentener, F.J., Dereczynski, C., Di Luca, A., Diongue Niang, A., Doblas-Reyes, F.J., Dosio, A.,

690   Douville, H., Engelbrecht, F., Eyring, V., Fischer, E., Forster, P., Fox-Kemper, B., Fuglestvedt, J.S., Fyfe, J.C., Gillett, N.P., Goldfarb, L., Gorodetskaya, I., Gutierrez, J.M., Hamdi, R., Hawkins, E., Hewitt, H.T., Hope, P., Islam, A.S., Jones, C., Kaufman, D.S., Kopp, R.E., Kosaka, Y., Kossin, J., Krakovska, S., Lee, J.-Y., Li, J., Mauritsen, T., Maycock, T.K., Meinshausen, M., Min, S.-K., Monteiro, P.M.S., Ngo-Duc, T., Otto, F., Pinto, I., Pirani, A., Raghavan, K., Ranasinghe, R., Ruane, A.C., Ruiz, L., Sallée, J.-B., Samset, B.H., Sathyendranath, S., Seneviratne, S.I., Sörensson, A.A., Szopa, S.,

695   Takayabu, I., Tréguier, A.-M., van den Hurk, B., Vautard, R., von Schuckmann, K., Zaehle, S., Zhang, X., and Zickfeld, K.: Technical Summary. In Climate Change 2021: The Physical Science Basis. Contribution of Working Group I to the Sixth Assessment Report of the Intergovernmental Panel on Climate Change, edited by Masson-Delmotte, V., Zhai, P., Pirani, A., Connors, S.L., Péan, C., Berger, S., Caud, N., Chen, Y., Goldfarb, L., Gomis, M.I., Huang, M., Leitzell, K., Lonnoy, E., Matthews, J.B.R., Maycock, T.K., Waterfield, T., Yelekçi, O., Yu, R., and Zhou, B., Cambridge University

700   Press, Cambridge, United Kingdom and New York, NY, USA, pp. 33−144, doi:10.1017/9781009157896.002, 2021.

Asano, S. and Shiobara, M.: Aircraft measurements of the radiative effects of tropospheric aerosols: I. Observational results of the radiation budget, J. Meteorol. Soc. Jpn., 67, 847–861, https://doi.org/10.2151/jmsj1965.67.5_847, 1989.

Chaikovsky, A., Dubovik, O., Holben, B., Bril, A., Goloub, P., Tanré, D., Pappalardo, G., Wandinger, U., Chaikovskaya, L., Denisov, S., Grudo, J., Lopatin, A., Karol, Y., Lapyonok, T., Amiridis, V., Ansmann, A., Apituley, A., Allados-Arboledas,

705   L., Binietoglou, I., Boselli, A., D'Amico, G., Freudenthaler, V., Giles, D., Granados-Muñoz, M. J., Kokkalis, P., Nicolae, D., Oshchepkov, S., Papayannis, A., Perrone, M. R., Pietruczuk, A., Rocadenbosch, F., Sicard, M., Slutsker, I., Talianu, C., De Tomasi, F., Tsekeri, A., Wagner, J., and Wang, X.: Lidar-Radiometer Inversion Code (LIRIC) for the retrieval of vertical aerosol properties from combined lidar/radiometer data: development and distribution in EARLINET, Atmos. Meas. Tech., 9, 1181–1205, https://doi.org/10.5194/amt-9-1181-2016, 2016.

710   Chang, H., and Charalampopoulos, T. T.: Determination of the wavelength dependence of refractive indices of flame soot, Proc. R. Soc. Lond., A 430, 577–591, https://doi.org/10.1098/rspa.1990.0107, 1990.

Dey, S., Tripathi, S. N., Singh, R. P., and Holben, B. N.: Retrieval of black carbon and specific absorption over Kanpur city, northern India during 2001-2003 using AERONET data, Atmos. Environ., 40, 445-456, https://doi.org/10.1016/j.atmosenv.2005.09.053, 2006.

715   Draine, B. T. and Flatau, P. J.: Discrete-Dipole Approximation For Scattering Calculations, J. Opt. Soc. Am. A, 11, 1491, https://doi.org/10.1364/JOSAA.11.001491, 1994

Dubovik, O., Holben, B., Eck, T. F., Smirnov, A., Kaufman, Y. J., King, M. D., Tanré, D., and Slutsker, I.: Variability of absorption and optical properties of key aerosol types observed in worldwide locations, J. Atmos. Sci., 59, 590–608, https://doi.org/10.1175/1520-0469(2002)059<0590:voaaop>2.0.co;2, 2002.

720   Dubovik, O., Sinyuk, A., Lapyonok, T., Holben, B. N., Mishchenko, M., Yang, P., Eck, T. F., Volten, H., Muñoz, O., Veilhelmann, B., van der Zande, W. J., Leon, J. F., Sorokin, M., and Slutsker, I.: Application of spheroid models to account for aerosol particle nonsphericity in remote sensing of desert dust, J. Geophys. Res., 111, D11208, https://doi.org/10.1029/2005JD006619, 2006.

Erickson III, D. J., and Duce, R. A.: On the global flux of atmosphere sea salt, J. Geophys. Res. 93, 14079-14088,
725   https://doi.org/10.1029/JC093iC11p14079, 1988.

Fujikawa, M., and Kudo, R., Nishizawa, T., Oikawa, E., Higrashi, A., and Okamoto, H.: Long-term analyses of aerosol optical thickness using CALIOP, Proceedings of EPJ Web of Conference, 237 (2020) 02023, The 29th International Laser Radar Conference (ILRC29), https://doi.org/10.1051/epjconf/202023702023, 2020.

Gelaro, R.,McCarty, W., Suárez, M.J., Todling, R., Molod, A., Takacs, L., Randles, C.A., Darmenov, A., Bosilovich, M.G.,
730   Reichle, R., Wargan, K., Coy, L., Cullather, R., Draper, C., Akella, S., Buchard, V., Conaty, A., da Silva, A.M., Gu, W., Kim, G.-K., Koster, R., Lucchesi, R., Merkova, D., Nielsen, J.E., Partyka, G., Pawson, S., Putman, W., Rienecker, M., Schubert, S.D., Sienkiewicz, M. and Zhao, B.: The Modern-Era Retrospective analysis for Research and Applications, version 2 (MERRA-2). Journal of Climate, 30(14), 5419–5454, 2017.

Getzewich, B. J., Vaughan, M. A., Hunt, W. H., Avery, M. A., Powell, K. A., Tackett, J. L., Winker, D. M., Kar, J., Lee, K.-
735   P., and Toth, T. D.: CALIPSO lidar calibration at 532 nm: version 4 daytime algorithm, Atmos. Meas. Tech., 11, 6309006326, https://doi.org/10.5194/amt-11-6309-2018, 2018.

Giles, D. M., Sinyuk, A., Sorokin, M. G., Schafer, J. S., Smirnov, A., Slutsker, I., Eck, T. F., Holben, B. N., Lewis, J. R., Campbell, J. R., Welton, E. J., Korkin, S. V., and Lyapustin, A. I.: Advancements in the Aerosol Robotic Network (AERONET) Version 3 database – automated near-real-time quality control algorithm with improved cloud screening for
740   Sun photometer aerosol optical depth (AOD) measurements, Atmos. Meas. Tech., 12, 169-209, https://doi.org/10.5194/amt-12-169-2019, 2019.

Hess, M., Koepke, P., and Schult, I.: Optical properties of aerosols and clouds: the software package OPAC, B. Am. Meteorol. Soc., 79, 831–844, 1998.

Higurashi, A., and Nakajima, T.: Detection of aerosol types over the East China sea near Japan from four-channel satellite
745   data, Geophys. Res. Lett., 29, 17, 1836, doi:10.1029/2002GL015357, 2002.

Holben, B. N., Eck, T. F., Slutsker, I., Tanré, D., Buis, J. P., Setzer, A., Vermote, E., Reagan, J. A., Kaufman, Y. J., Nakajima, T., Lavenu, F., Jankowiak, I., and Smirnov, A.: AERONET – A federated instrument network and data archive for aerosol characterization, Remote Sens. Environ., 66, 1–16, https://doi.org/10.1016/S0034-4257(98)00031-5, 1998.

Illingworth, A. J., Barker, H. W., Beljaars, A., Ceccaldi, M., Chepfer, H., Clerbaux, N., Cole, J. Delanoë, J., Domenech, C.,
750   Donovan, D. P., Fukuda, S., Hirakata, M., J. Hogan, R., Huenerbein, A., Kollias, P., Kubota, T., Nakajima, T., Nakajima, T. Y., Nishizawa, T., Ohno, Y., Okamoto, H., Oki, R., Sato, K., Satoh, M., Shephard, M. W., Velázquez-Blázquez, A., Wandinger, U., Wehr, T., Van Zadelhoff G. J.: The EarthCARE satellite: The next step forward in global measurements

of clouds, aerosols, precipitation, and radiation, Bull. Am. Meteor. Soc., 96, 1311-1332, https://doi.org/10.1175/BAMS-D-12-00227.1, 2015.

755 Ishimoto, H., Zaizen, Y., Uchiyama, A., Masuda, K., and Mano, Y.: Shape modeling of mineral dust particles for light-scattering calculations using the spatial Poisson–Voronoi tessellation, J. Quant. Spectrosoc. Radiat. Transfer, 111, 16, 2434-2443, https://doi.org/10.1016/j.jqsrt.2010.06.018, 2010.

Ishimoto, H., Masuda, K., Mano, Y., Orikasa, N., and Uchiyama, A.: Irregularly shaped ice aggregates in optical modeling of convectively generated ice clouds, J. Quant. Spectrosc. Ra., 113, 632–643, https://doi.org/10.1016/j.jqsrt.2012.01.017, 760 2012.

Ishimoto, H., Kudo, R., and Adachi, K.: A shape model of internally mixed soot particles derived from artificial surface tension, Atmos. Meas. Tech., 12, 107–118, https://doi.org/10.5194/amt-12-107-2019, 2019.

Jin, Y., Nishizawa, T., Sugimoto, N., Takakura, S., Aoki, M., Ishii, S., Yamazaki, A., Kudo, R., Yumimoto, K., Sato, K., and Okamoto, H.: Demonstration of aerosol profile measurement with a dual-wavelength high-spectral-resolution lidar using 765 a scanning interferometer, Appl. Opt., 61, 3523-3532, https://doi.org/10.1364/AO.451707, 2022.

Kahnert, M., Nousiainen, T., Lindqvist, H., and Ebert, M.: Optical properties of light absorbing carbon aggregates mixed with sulfate: assessment of different model geometries for climate forcing calculations, Opt. Express, 20, 10042-10058, https://doi.org/10.1364/OE.20.010042, 2012.

Kahnert, M., Nousiainen, T., and Lindqvist, H.: Models for integrated and differential scattering optical properties of 770 encapsulated light absorbing carbon aggregates, Opt. Express, 21, 7974-7933, https://doi.org/10.1364/OE.21.007974, 2013.

Kar, J., Vaughan, M. A., Lee, K.-P., Tackett, J. L., Avery, M. A., Garnier, A., Getzewich, B. J., Hunt, W. H., Josset, D., Liu, Z., Lucker, P. L., Magill, B., Omar, A. H., Pelon, J., Rogers, R. R., Toth, T. D., Trepte, C. R., Vernier, J.-P., Winker, D. M., and Young, S. A.: CALIPSO lidar calibration at 532?nm: version 4 nighttime algorithm, Atmos. Meas. Tech., 11, 1459–1479, https://doi.org/10.5194/amt-11-1459-2018, 2018.

775 Kaufman, Y. J., Tanré, D., Léon, J.-F., and Pelon, J.: Retrievals of profiles of fine and coarse aerosols using lidar and radiometric space measurements, IEEE Transactions on Geoscience and Remote Sensing, 41, 8, 1743-1754, doi:10.1109/TGRS.2003.814138, 2003.

Kim, J., Lee, J., Lee, H. C., Higurashi, A., Takemura, T., and Song, C. H.: Consistency of the aerosol type classification from satellite remote sensing during the atmospheric brown cloud-East Asia regional experiment campaign, J. Geophys. Res., 780 112, D22S33, doi:10.1029/2006JD008201, 2007.

Kim, M.-H., Omar, A. H., Tackett, J. L., Vaughan, M. A., Winker, D. M., Trepte, C. R., Hu, Y., Liu, Z., Poole, L. R., Pitts, M. C., Kar, J., and Magill, B. E.: The CALIPSO version 4 automated aerosol classification and lidar ratio selection algorithm, Atmos. Meas. Tech., 11, 6107–6135, https://doi.org/10.5194/amt-11-6107-2018, 2018.

Kinne, S.: Aerosol radiative effects with MACv2, Atmos. Chem. Phys., 19, 10919–10959, https://doi.org/10.5194/acp-19-785 10919-2019, 2019.

Korras-Carraca, M. B., Pappas, V., Hatzianastassiou, N., Vardavas, I., Matsoukas, C.: Global vertically resolved aerosol direct radiation effect from three years of CALIOP data using the FORTH radiation transfer model, Atmos. Res., 224, 138-156, https://doi.org/10.1016/j.atmosres.2019.03.024, 2019.

Kudo, R., Uchiyama, A., Yamazaki, A., Sakami, T., and Kobayashi, E.: From solar radiation measurements to optical properties: 1998-2008 trends in Japan, Geophys. Res. Lett., 37, L04805, doi:10.1029/2009GL041794, 2010a.

Kudo, R., Uchiyama, A., Yamazaki, A., and Kobayashi, E.: Seasonal characteristics of aerosol radiative effect estimated from ground-based solar radiation measurements in Tsukuba, Japan, J. Geophys. Res., 115, D01204, doi:10.1029/2009JD012487, 2010b.

Kudo, R., Uchiyama, A., Yamazaki, A., Sakami, T., and Ijima, O.: Decadal changes in aerosol optical thickness and single scattering albedo estimated from ground-based broadband radiometers: A case study in Japan, J. Geophys. Res., 116, D03207, https://doi.org/10.1029/2010JD014911, 2011.

Kudo, R., Nishizawa, T., and Aoyagi, T.: Vertical profiles of aerosol optical properties and the solar heating rate estimated by combining sky radiometer and lidar measurements, Atmos. Meas. Tech., 9, 3223–3243, https://doi.org/10.5194/amt-9-3223-2016, 2016.

Kudo, R., Diémoz, H., Estellés, V., Campanelli, M., Momoi, M., Marenco, F., Ryder, C. L., Ijima, O., Uchiyama, A., Nakashima, K., Yamazaki, A., Nagasawa, R., Ohkawara, N., and Ishida, H.: Optimal use of the Prede POM sky radiometer for aerosol, water vapor, and ozone retrievals, Atmos. Meas. Tech., 14, 3395–3426, https://doi.org/10.5194/amt-14-3395-2021, 2021.

Lewis, E. R., and Schwartz, S. E.: Fundamentals in "Sea salt aerosol production: mechanisms, methods, measurements and models", Geophysical Monograph Series, American Geophysical Union, 152, 9-99, ISBN:9781118666050, doi:10.1029/GM152, 2004.

Li, M., Liu, J., Wang, Z., Wang, H., Zhang, Z., Zhang, L., and Yang, Q.: Assessment of sea surface wind from NWP reanalysis and satellites in the southern ocean, 1842-1853, https://doi.org/10.1175/JTECH-D-12-00240.1, 2013.

Liu, Z., M. A. Vaughan, D. M. Winker, C. Kittaka, B. J. Getzewich, R. E. Kuehn, A. Omar, K. Powell, C. R. Trepte, and C. A. Hostetler: The CALIPSO lidar cloud and aerosol discrimination: Version 2 algorithm and initial assessment of performance, J. Atmos. Oceanic Technol., 26, 1198–1213, 2009.

Liu, Z., Kar, J., Zeng, S., Tackett, J., Vaughan, M., Avery, M., Pelon, J., Getzewich, B., Lee, K.-P., Magill, B., Omar, A., Lucker, P., Trepte, C., and Winker, D.: Discriminating between clouds and aerosols in the CALIOP version 4.1 data products, Atmos. Meas. Tech., 12, 703–734, https://doi.org/10.5194/amt-12-703-2019, 2019.

Lopatin, A., Dubovik, O., Chaikovsky, A., Goloub, P., Lapyonok, T., Tanré, D., and Litvinov, P.: Enhancement of aerosol characterization using synergy of lidar and sun-photometer coincident observations: the GARRLiC algorithm, Atmos. Meas. Tech., 6, 2065–2088, https://doi.org/10.5194/amt-6-2065-2013, 2013.

Matsui, H., Koike, M., Kondo, Y., Moteki, N., Fast, J. D., and Zaveri, R. A.: Development and validation of a black carbon missing state resolved three-dimensional model: Aging process and radiative impact, J. Geophys. Res. 118, 2304-2326, https://doi.org/10.1029/2012JD018446, 2013.

Matsui, H., Hamilton, D. S. and Mahowald, N. M.: Black carbon radiative effects highly sensitive to emitted particle size when resolving mixing-state diversity, Nat. Commun., 9, 3446, https://doi.org/10.1038/s41467-018-05635-1, 2018.

Maxwell Garnet, J. C.: Colours in metal glasses and in metallic films, Philos. Trans. R. Soc., A 203, 283-420, 1904.

Nakajima, T., and Tanaka, M.: Effect of wind-generated waves on the transfer of solar radiation in the atmosphere-ocean system, J. Quant. Spectrosoc. Radiant. Transfer, 29, 6, 521-537, https://doi.org/10.1016/0022-4073(83)90129-2, 1983.

Nakajima, T., Campanelli, M., Che, H., Estellés, V., Irie, H., Kim, S.-W., Kim, J., Liu, D., Nishizawa, T., Pandithurai, G., Soni, V. K., Thana, B., Tugjsurn, N.-U., Aoki, K., Go, S., Hashimoto, M., Higurashi, A., Kazadzis, S., Khatri, P., Kouremeti, N., Kudo, R., Marenco, F., Momoi, M., Ningombam, S. S., Ryder, C. L., Uchiyama, A., and Yamazaki, A.: An overview of and issues with sky radiometer technology and SKYNET, Atmos. Meas. Tech., 13, 4195–4218, https://doi.org/10.5194/amt-13-4195-2020, 2020.

Nishizawa, T., Asano, S., Uchiyama, A., and Yamazaki, A.: Seasonal variation of aerosol direct radiative forcing and optical properties estimated from ground-based solar radiation measurements, J. Atmos. Sci., 61, 57–72, https://doi.org/10.1175/1520-0469(2004)061<0057:SVOADR>2.0.CO;2, 2004.

Nishizawa, T., Okamoto, H., Sugimoto, N., Matsui, I., Shimizu, A, and Aoki, K.: An algorithm that retrieves aerosol properties from dual-wavelength polarized lidar measurements, J. Geophys. Res., 112, D06212, https://doi.org/10.1029/2006JD007435, 2007.

Nishizawa, T., Sugimoto, N., Matsui, I., Shimizu, A., Tatarov, B., Okamoto, H.: Algorithm to retrieve aerosol optical properties from High-Spectral-Resolution-Lidar and polarization Mie-Scattering Lidar measurements, IEEE Trans. Geosci. Remote Sensing, 46 (12), 4094-4103, https://doi.org/10.1109/TGRS.2008.2000797, 2008.

Nishizawa, T., Sugimoto, N., Matsui, I., Shimizu, A., and Okamoto, H.: Algorithms to retrieve optical properties of three component aerosols from two-wavelength backscatter and one-wavelength polarization lidar measurements considering nonsphericity of dust, J. Quant. Spectrosoc. Radiat. Transfer, 112, 2, 254-267, https://doi.org/10.1016/j.jqsrt.2010.06.002, 2011.

Nishizawa, T., Sugimoto, N., Matsui, I., Shimizu, A., Hara, Y., Uno, I., Yasunaga, K., Kudo, R., and Kim, S.-W.: Ground-based network observation using Mie-Raman lidars and multi-wavelength Raman lidars and algorithm to retrieve distributions of aerosol components, J. Quant. Spectrosoc. Radiat. Transfer, 188, 79-93, https://doi.org/10.1016/j.jqsrt.2016.06.031, 2017.

Omar, A. H., Winker, D. M., Kittaka, C., Vaughan, M. A., Liu, Z., Hu, Y., Trepte, C. R., Rogers, R. R., Ferrare, R. A., Lee, K.-P., Kuehn, R. E., and Hostetler, C. A.: The CALIPSO automated aerosol classification and lidar ratio selection algorithm, J. Atmos. Ocean. Tech., 26, 1994–2014, https://doi.org/10.1175/2009JTECHA1231.1, 2009.

Omar, A. H., Winker, D. M., Tackett, J. L., Giles, D. M., Kar, J., Liu, Z., Vaughan, M. A., Powell, K. A., and Trepte, C. R.: CALIOP and AERONET aerosol optical depth comparisons: one size fits none, J. Geophys. Res., 118, 4748-4766, doi:10.1002/jgrd.50330, 2013.

Ota, Y., Higurashi, A., Nakajima, T., and Yokota, T.: Matrix formulations of radiative transfer including the polarization effect
855   in a coupled atmosphere-ocean system, J. Quant. Spectrosoc. Radiat. Transfer, 111, 6, 878-894, https://doi.org/10.1016/j.jqsrt.2009.11.021, 2010.

Platnick, S., King, M., and Hubanks, P.: MODIS Atmosphere L3 Monthly Product. NASA MODIS Adaptive Processing System, Goddard Space Flight Center [data set], USA, https://doi.org/10.5067/MODIS/MYD08_M3.061, 2015.

Redemann, J., Wood, R., Zuidema, P., Doherty, S. J., Luna, B., LeBlanc, S. E., Diamond, M. S., Shinozuka, Y., Chang, I. Y.,
860   Ueyama, R., Pfister, L., Ryoo, J.-M., Dobracki, A. N., da Silva, A. M., Longo, K. M., Kacenelenbogen, M. S., Flynn, C. J., Pistone, K., Knox, N. M., Piketh, S. J., Haywood, J. M., Formenti, P., Mallet, M., Stier, P., Ackerman, A. S., Bauer, S. E., Fridlind, A. M., Carmichael, G. R., Saide, P. E., Ferrada, G. A., Howell, S. G., Freitag, S., Cairns, B., Holben, B. N., Knobelspiesse, K. D., Tanelli, S., L'Ecuyer, T. S., Dzambo, A. M., Sy, O. O., McFarquhar, G. M., Poellot, M. R., Gupta, S., O'Brien, J. R., Nenes, A., Kacarab, M., Wong, J. P. S., Small-Griswold, J. D., Thornhill, K. L., Noone, D., Podolske, J.
865   R., Schmidt, K. S., Pilewskie, P., Chen, H., Cochrane, S. P., Sedlacek, A. J., Lang, T. J., Stith, E., Segal-Rozenhaimer, M., Ferrare, R. A., Burton, S. P., Hostetler, C. A., Diner, D. J., Seidel, F. C., Platnick, S. E., Myers, J. S., Meyer, K. G., Spangenberg, D. A., Maring, H., and Gao, L.: An overview of the ORACLES (ObseRvations of Aerosols above CLouds and their intEractionS) project: aerosol–cloud–radiation interactions in the southeast Atlantic basin, Atmos. Chem. Phys., 21, 1507–1563, https://doi.org/10.5194/acp-21-1507-2021, 2021.

870 Rogers, R. R., Hostetler, C. A., Hair, J. W., Ferrare, R. A., Liu, Z., Obland, M. D., Harper, D. B., Cook, A. L., Powell, K. A., Vaughan, M. A., and Winker, D. M.: Assessment of the CALIPSO Lidar 532 nm attenuated backscatter calibration using the NASA LaRC airborne High Spectral Resolution Lidar, Atmos. Chem. Phys., 11, 1295–1311, https://doi.org/10.5194/acp-11-1295-2011, 2011.

Schaaf, C. B., Gao, F., Strahler, A. H., Lucht, W., Li, X., Tsang, T., Strugnell, N. C., Zhang, X., Jin, Y., Muller, J.-P., Lewis,
875   P., Barnsley, M., Hobson, P., Disney, M., Roberts, G., Dunderdale, M., Doll, C., d'Entremont, R. P., Hu, B., Liang, S., Privette, J. L., and Roy, D.: First operational BRDF, albedo nadir reflectance products from MODIS, Remote Sens. Environ., 83, 135-148, https://doi.org/10.1016/S0034-4257(02)00091-3, 2002.

Schuster, G. L., Dubovik, O., and Holben, B. N.: Inferring black carbon content and specific absorption from Aerosol Robotic Network (AERONET) aerosol retrievals, J. Geophys. Res., 110, D10S17, doi:10.1029/2004JD004548, 2005.

880 Schuster, G. L., Vaughan, M., MacDonnell, D., Su, W., Winker, D., Dubovik, O., Lapyonok, T., and Trepte, C.: Comparison of CALIPSO aerosol optical depth retrievals to AERONET measurements, and a climatology for the lidar ratio of dust, Atmos. Chem. Phys., 12, 7431-7452, doi:10.5194/acp-12-7431-2012, 2012.

Sekiguchi, M. and Nakajima, T.: A k-distribution-based radiation code and its computational optimization for an atmospheric general circulation model, J. Quant. Spectrosc. Ra., 109, 2779–2793, https://doi.org/10.1016/j.jqsrt.2008.07.013, 2008.

885   Shimizu, A., Nishizawa, T., Jin, Y., Kim, S-W., Wang, Z., Batdorj, D., and Sugimoto, N.: Evolution of a lidar network for tropospheric aerosol detection in East Asia, Optical Engineering 56 (3), 031219, https://doi.org/10.1117/1.OE.56.3.031219, 2016.

Sinyuk, A., Holben, B. N., Eck, T. F., Giles, D. M., Slutsker, I., Korkin, S., Schafer, J. S., Smirnov, A., Sorokin, M., and Lyapustin, A.: The AERONET Version 3 aerosol retrieval algorithm, associated uncertainties and comparisons to Version

890   2, Atmos. Meas. Tech., 13, 3375–3411, https://doi.org/10.5194/amt-13-3375-2020, 2020.

Stroeve, J., Box, J. E., Gao, F., Liang, S., Nolin, A., and Schaaf, C.: Accuracy assessment of the MODIS 16-day albedo product for snow: comparisons with Greenland in situ measurements, Remote Sens. Environ., 94, 1, 46-60, https://doi.org/10.1016/j.rse.2004.09.001, 2005.

Stroeve, J., Box, J. E., Wang, Z., Schaaf, C., Barrett, A.: Re-evaluation of MODIS MCD43 Greenland albedo accuracy and

895   trends, Remote Sens. Environ., 138, https://doi.org/10.1016/j.rse.2013.07.023, 2013.

Sugimoto, N., Nishizawa, T., Shimizu, A., Matsui, I., Higurashi, A., Uno, I., Hara, Y., Yumimoto, K., and Kudo, R.: Continuous observations of atmospheric aerosols across East Asia, SPIE Newsroom, 21 October, doi:10.1117/2.1201510.006178, 2015.

Tackett, J. L., Winker, D. M., Getzewich, B. J., Vaughan, M. A., Young, S. A., and Kar, J.: CALIPSO lidar level 3 aerosol

900   profile product: version 3 algorithm design, Atmos. Meas. Tech., 11, 4129–4152, https://doi.org/10.5194/amt-11-4129-2018, 2018.

Vaughan, M., Garnier, A., Josset, D., Avery, M., Lee, K.-P., Liu, Z., Hunt, W., Pelon, J., Hu, Y., Burton, S., Hair, J., Tackett, J. L., Getzewich, B., Kar, J., and Rodier, S.: CALIPSO lidar calibration at 1064 nm: version 4 algorithm, Atmos. Meas. Tech., 12, 51–82, https://doi.org/10.5194/amt-12-51-2019, 2019.

905   Wang, Z., Schaaf, C. B., Strahler, A. H., Chopping, M. J., Román, M. O., Shuai, Y., Woodcock, C. E., Hollinger, D. Y., Fitzjarrald, D. R.: Evaluation of MODIS albedo product (MCD43A) over grassland, agriculture and forest surface types during dormant and snow-covered periods, Remote Sens. Environ., 140, 60-77, https://doi.org/10.1016/j.rse.2013.08.025, 2014.

Wang, Z., Schaaf, C.B., Sun, Q., Shuai, Y., Román, M.O.: Capturing rapid land surface dynamics with Collection V006

910   MODIS   BRDF/NBAR/Albedo   (MCD43)   products,   Remote   Sensing   of   Environment   207,   50-64, https://doi.org/10.1016/j.rse.2018.02.001, 2018.

Williamson, S. N., Copland, L., Hik, D. S.: The accuracy of satellite-derived albedo for northern alpine and glaciated land covers, Polar Science, 10, 3, 262-269, https://doi.org/10.1016/j.polar.2016.06.006, 2016.

Winker, D. M., Pelon, J., Coakley, Jr., J. A., Ackerman, S. A., Charlson, R. J., Colarco, P. R., Flamant, P., Fu, Q., Hoff, R. M.,

915   Kittaka, C., Kubar, T. L., Le Treut, H., McCormick, M. P., Megie, G., Poole, L., Powell, K., Trepte, C., Vaughan, M. A., and Wielicki, B. A.: The CALIPSO mission: A Global 3D view of aerosols and clouds, B. Am. Meteorol. Soc., 91, 1211–1229, https://doi.org/10.1175/2010BAMS3009.1, 2010.

Xu, F., Gao, L., Redemann, J., Flynn, C. J., Espinosa, W. R., da Silva, A. M., Stamnes, S., Burton, S. P., Liu, X., Ferrare, R.,
Cairns, B., and Dubovik, O.: A combined lidar-polarimeter inversion approach for aerosol remote sensing over ocean,
920   Front. Remote. Sens., 21, https://doi.org/10.3389/frsen.2021.620871, 2021.

Table 1. Physical and optical properties of the four aerosol component at relative humidities of 0 and 80 % (0/80 %).

Aerosol component	Median radius (μm)	Single-scattering albedo at 532 nm	Asymmetry factor at 532 nm	Lidar ratio at 532 nm (steradians)	Linear depolarization ratio at 532 nm
Water-soluble	0.10/0.14	0.96/0.98	0.50/0.63	40/60	0.00/0.00
Light-absorbing (Core-grey shell, 30 %*)	0.10/0.13	0.44/0.64	0.46/0.59	77/92	0.00/0.00
Light-absorbing (Core-grey shell, 15 %*)	0.10/0.14	0.58/0.79	0.47/0.61	61/77	0.00/0.00
Light-absorbing (Homogeneous internal mixture, 30 %*)	0.10/0.13	0.46/0.65	0.49/0.60	88/99	0.00/0.00
Light-absorbing (Core-shell 30 %*)	0.10/0.13	0.43/0.61	0.43/0.53	67/66	0.00/0.00
Dust (Voronoi)	2.00/2.00	0.91/0.91	0.71/0.71	41/41	0.49/0.49
Dust (Spheroid)	2.00/2.00	0.92/0.92	0.76/0.76	51/51	0.30/0.30
Sea salt	2.00/3.99	1.00/1.00	0.72/0.80	13/19	0.00/0.00

*Volume fraction of black carbon in a particle.

925

Table 2. Aerosol components and median radius (DMR) values used in the simulations of CALIOP and MODIS observations.

Case	Aerosols in the boundary layer	Aerosols in the free atmosphere	DMRs of fine (WS, LA)/coarse (DS) particles (µm)
Land Average	External mixture of WS, LA, DS	No aerosols	0.10/2.00
Land Dust 1	External mixture of WS, LA, DS	DS	0.10/2.00
Land Dust 2	External mixture of WS, LA, DS	DS	0.10/1.00
Land Dust 3	External mixture of WS, LA, DS	DS	0.10/4.00
Land Biomass-Burning 1	External mixture of WS, LA, DS	External mixture of WS, LA	0.10/2.00
Land Biomass-Burning 2	External mixture of WS, LA, DS	External mixture of WS, LA	0.07/2.00
Land Biomass-Burning 3	External mixture of WS, LA, DS	External mixture of WS, LA	0.15/2.00
Land Polluted Dust	External mixture of WS, LA, DS	External mixture of WS, LA, DS	0.10/2.00
Ocean Clean	External mixture of WS, SS	No aerosols	0.10/2.00
Ocean Dust 1	External mixture of WS, SS	DS	0.10/2.00
Ocean Dust 2	External mixture of WS, SS	DS	0.10/1.00
Ocean Dust 3	External mixture of WS, DS	DS	0.10/4.00
Ocean Biomass-Burning 1	External mixture of WS, DS	External mixture of WS, LA	0.10/2.00
Ocean Biomass-Burning 2	External mixture of WS, DS	External mixture of WS, LA	0.07/2.00
Ocean Biomass-Burning 3	External mixture of WS, DS	External mixture of WS, LA	0.15/2.00
Ocean Polluted Dust	External mixture of WS, DS	External mixture of WS, LA, DS	0.10/2.00

Table 3. Means and standard deviations of differences of columnar properties between retrievals and simulations.

Parameter	Aerosol optical depth at 532 nm	Land		Ocean	
		532 nm	1064 nm	532 nm	1064 nm
Aerosol optical depth (relative value)	<0.3	−0.02 ± 0.10	0.00 ± 0.14	−0.15 ± 0.25	−0.10 ± 0.10
	≥0.3	−0.03 ± 0.11	−0.02 ± 0.13	0.10 ± 0.13	0.06 ± 0.11
Aerosol optical depth of water-soluble particles (relative value)	<0.3	−0.09 ± 0.15		−0.31 ± 0.39	
	≥0.3	−0.04 ± 0.12		0.05 ± 0.23	
Aerosol optical depth of light-absorbing particles (relative value)	< 0.3	1.14 ± 1.31		0.27 ± 0.86	
	≥0.3	0.24 ± 0.99		0.78 ± 0.85	
Aerosol optical depth of dust (relative value)	<0.3	0.15 ± 1.67		−0.17 ± 0.11	
	≥0.3	0.05 ± 1.53		−0.09 ± 0.08	
Aerosol optical depth of sea salt (relative value)	<0.3			0.41 ± 0.50	
	≥0.3			−0.02 ± 0.30	
Single-scattering albedo (absolute value)	<0.3	−0.02 ± 0.05	−0.01 ± 0.08	−0.01 ± 0.04	0.01 ± 0.06
	≥0.3	−0.01 ± 0.03	−0.01 ± 0.04	−0.03 ± 0.04	−0.03 ± 0.05
Asymmetry factor (absolute value)	<0.3	0.02 ± 0.03	0.00 ± 0.03	0.03 ± 0.04	0.04 ± 0.05
	≥0.3	0.01 ± 0.02	0.00 ± 0.02	0.00 ± 0.02	−0.02 ± 0.04
Dry median radius of fine particles (relative value)	<0.3	0.09 ± 0.10		0.04 ± 0.11	
	≥0.3	0.04 ± 0.08		0.03 ± 0.08	
Dry median radius of coarse particles (relative value)	<0.3	0.08 ± 0.27		0.11 ± 0.39	
	≥0.3	0.06 ± 0.18		0.06 ± 0.15	

930

Table 4. Means and standard deviations of differences of vertically resolved properties between retrievals and simulations.

Parameter at 532 nm	Aerosol optical depth at 532 nm	Land	Ocean
Extinction coefficient (relative error)	<0.3	−0.04 ± 0.19	−0.17 ± 0.35
	≥0.3	−0.04 ± 0.16	0.09 ± 0.26
Extinction coefficient of water-soluble (relative error)	<0.3	−0.15 ± 0.30	−0.35 ± 0.54
	≥0.3	−0.07 ± 0.22	0.06 ± 0.42
Extinction coefficient of light-absorbing (relative error)	<0.3	1.85 ± 3.66	0.11 ± 0.84
	≥0.3	0.30 ± 1.72	0.54 ± 0.95
Extinction coefficient of dust (relative error)	<0.3	−0.06 ± 1.50	−0.18 ± 0.13
	≥0.3	−0.05 ± 1.28	−0.10 ± 0.10
Extinction coefficient of sea salt (relative error)	<0.3		0.37 ± 0.46
	≥0.3		−0.02 ± 0.34
Single-scattering albedo (absolute error)	<0.3	−0.03 ± 0.09	−0.01 ± 0.05
	≥0.3	−0.01 ± 0.05	−0.03 ± 0.06
Asymmetry factor (absolute error)	<0.3	0.02 ± 0.03	0.04 ± 0.06
	≥0.3	0.01 ± 0.02	0.00 ± 0.03

935

Table 5. Means and standard deviations of deviations of the retrieval results using different particle models compared with the retrieval result using the Voronoi model for dust and the core-grey shell 30 %* model for light-absorbing particles.

Parameter	Spheroid for dust	Core-grey shell 15%* for light-absorbing	Homogeneous mixture 30%* for light-absorbing particles	Core-shell 30%* for light-absorbing particles
Aerosol optical depth of water-soluble particles at 532 nm	−0.005 ± 0.019	−0.004 ± 0.012	0.001 ± 0.008	−0.005 ± 0.013
Aerosol optical depth of light-absorbing particles at 532 nm	−0.004 ± 0.009	−0.006 ± 0.011	0.002 ± 0.006	−0.008 ± 0.013
Aerosol optical depth of dust at 532 nm	0.015 ± 0.038	0.000 ± 0.005	0.000 ± 0.003	0.000 ± 0.004
Aerosol optical depth of sea salt at 532 nm	−0.002 ± 0.005	0.001 ± 0.005	0.000 ± 0.004	0.001 ± 0.003
Dry median radius of fine particles (μm)	−0.002 ± 0.004	0.001 ± 0.003	0.000 ± 0.002	0.001 ± 0.004
Dry median radius of coarse particles (μm)	−0.071 ± 0.109	0.029 ± 0.096	0.005 ± 0.060	0.016 ± 0.089

*Volume fraction of black carbon in a particle.

940 **Table A1. Objective function (Eq. (A1)) for different volume fractions of BC core (f_{core}) in a particle, volume-equivalent sphere radius ranges, and wavelengths. Bold underlined text indicates the minimum value of the objective function in each row.**

Radius (µm)	Wavelength (µm)	f_{core}										
		0.0	0.1	0.2	0.3	0.4	0.5	0.6	0.7	0.8	0.9	1.0
<0.1	0.340	0.038	0.038	0.038	0.038	0.037	0.035	0.032	0.027	**_0.021_**	0.022	0.037
	0.355	0.039	0.039	0.038	0.037	0.036	0.033	0.029	0.024	**_0.017_**	0.019	0.038
	0.380	0.047	0.047	0.047	0.045	0.043	0.039	0.032	0.024	**_0.014_**	0.017	0.040
	0.400	0.059	0.059	0.058	0.057	0.053	0.048	0.040	0.029	0.017	**_0.015_**	0.039
	0.500	0.064	0.064	0.064	0.062	0.058	0.053	0.044	0.032	0.021	**_0.016_**	0.035
	0.532	0.064	0.064	0.063	0.062	0.058	0.053	0.044	0.033	0.022	**_0.017_**	0.033
	0.675	0.053	0.053	0.053	0.051	0.048	0.043	0.036	0.028	0.021	**_0.020_**	0.032
	0.870	0.045	0.045	0.044	0.043	0.041	0.038	0.034	0.031	**_0.029_**	0.032	0.042
	1.020	0.050	0.050	0.050	0.049	0.047	0.045	0.042	0.041	**_0.040_**	0.045	0.055
	1.064	0.053	0.053	0.053	0.052	0.051	0.049	0.047	0.046	**_0.045_**	0.051	0.062
≥0.1	0.340	0.142	0.142	0.142	0.140	0.136	0.128	0.114	0.092	0.060	**_0.049_**	0.158
	0.355	0.124	0.124	0.124	0.122	0.118	0.111	0.098	0.077	**_0.050_**	0.052	0.149
	0.380	0.092	0.092	0.092	0.091	0.087	0.081	0.070	0.054	**_0.038_**	0.060	0.137
	0.400	0.072	0.072	0.072	0.071	0.068	0.062	0.053	0.041	**_0.034_**	0.062	0.126
	0.500	0.039	0.039	0.039	0.038	0.035	0.032	0.027	**_0.027_**	0.037	0.061	0.099
	0.532	0.035	0.035	0.035	0.034	0.032	0.029	**_0.026_**	0.027	0.037	0.057	0.090
	0.675	0.035	0.035	0.035	0.034	0.032	0.030	**_0.029_**	0.030	0.034	0.046	0.067
	0.870	0.041	0.041	0.041	0.040	0.039	0.038	**_0.037_**	0.037	0.041	0.051	0.067
	1.020	0.048	0.048	0.048	0.048	0.047	**_0.047_**	0.047	0.049	0.055	0.067	0.086
	1.064	0.050	0.050	0.050	0.050	0.050	**_0.049_**	0.050	0.052	0.058	0.071	0.092
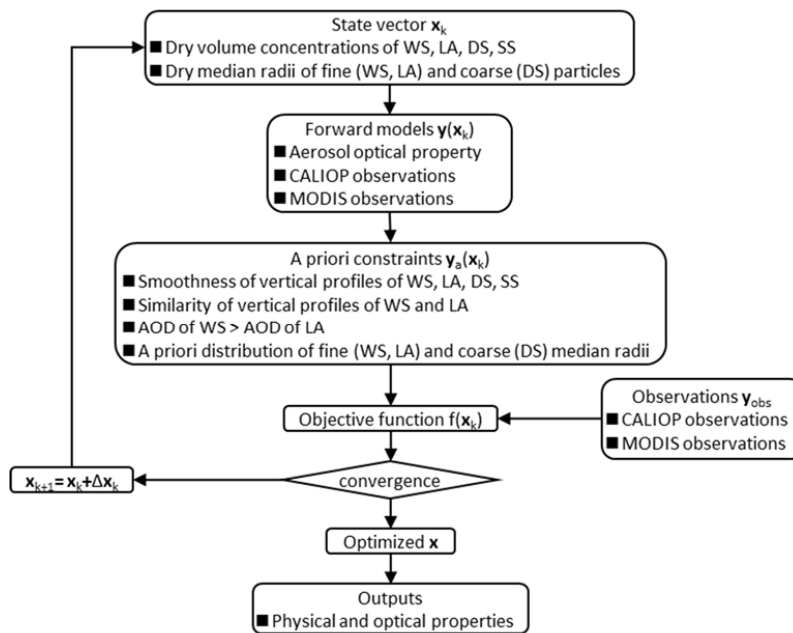
945 **Figure 1. Schematic diagram of the retrieval procedures.**
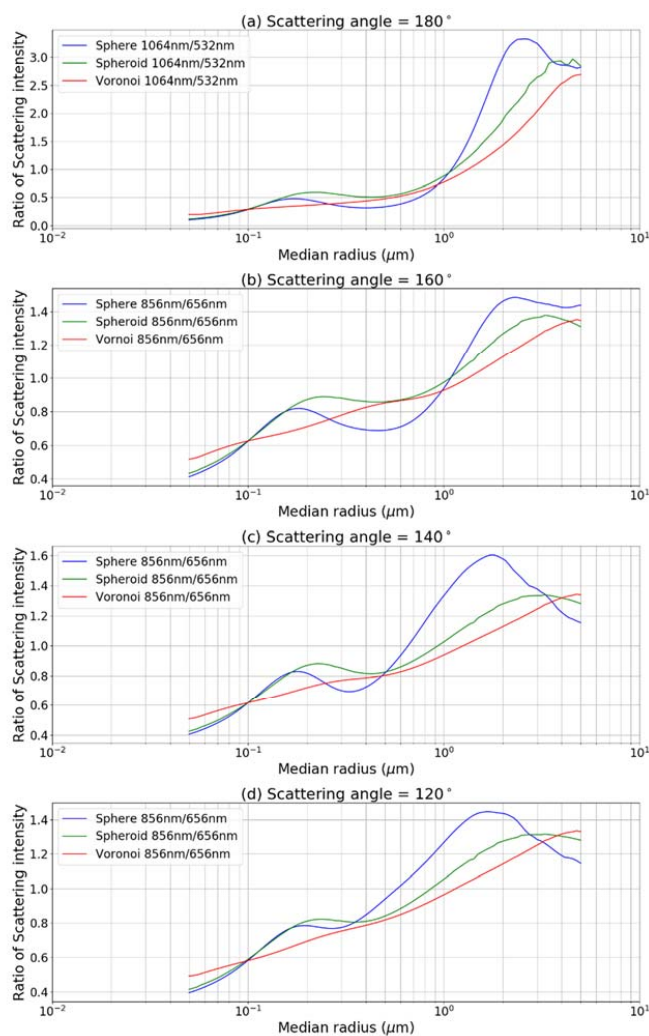
Figure 2. Relation between median radius and the ratio of scattering intensity at different wavelengths for (a) CALIOP and (b, c, and d) MODIS observations. Blue, green, and red colours indicate sphere, spheroid, and Voronoi particle models, respectively.

950
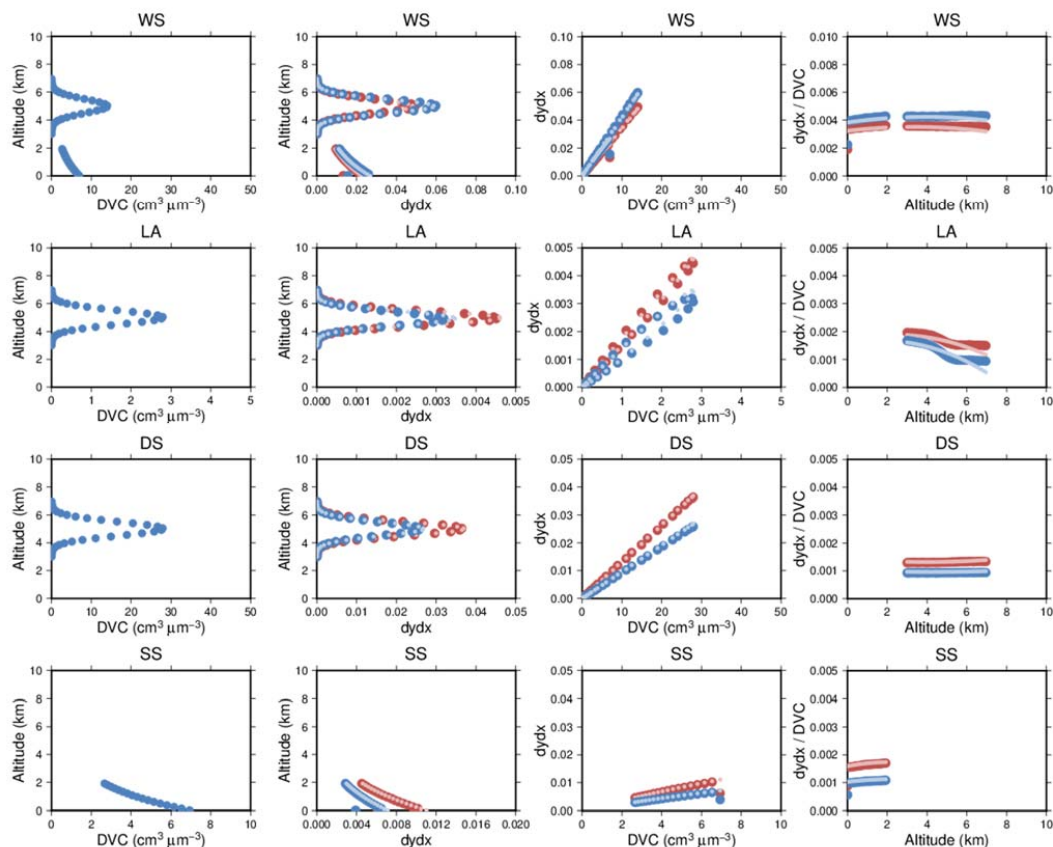
Figure 3. Approximation of the numerical derivatives of MODIS radiances for the DVCs of WS (first row), LA (second row), DS (third row), and SS (fourth row). The first column shows vertical profiles of DVC; the second column shows vertical profiles of the numerical derivatives (dydx); the third column shows the dependency of dydx on DVC; and the fourth column shows the dependency of dydx/DVC on altitude. Blue and red colours indicate dydx at MODIS bands 1 and 2, respectively. Dark and light colours indicate the reference values and the approximated calculations, respectively.

955
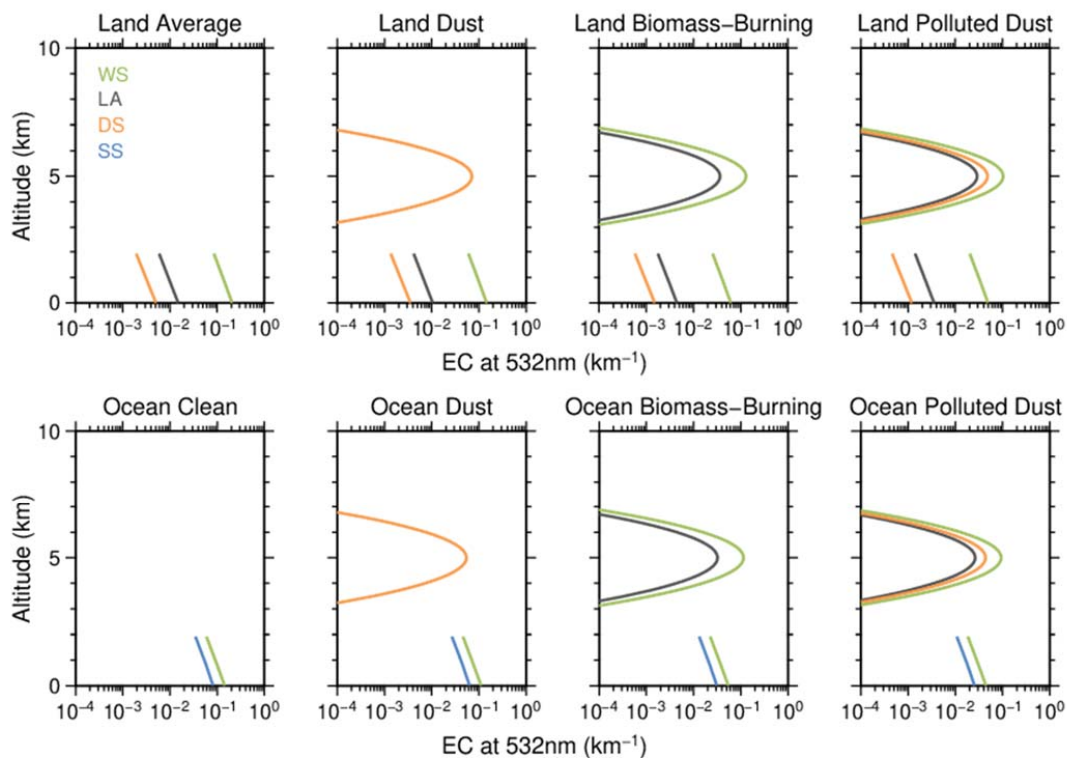
Figure 4. Vertical profiles of the EC of WS (green), LA (black), DS (orange), and SS (blue) used in the simulations of the clean, average, dust, biomass-burning, and polluted dust cases over land and ocean surfaces. Total AOD in all panels is 0.3 at 532 nm.
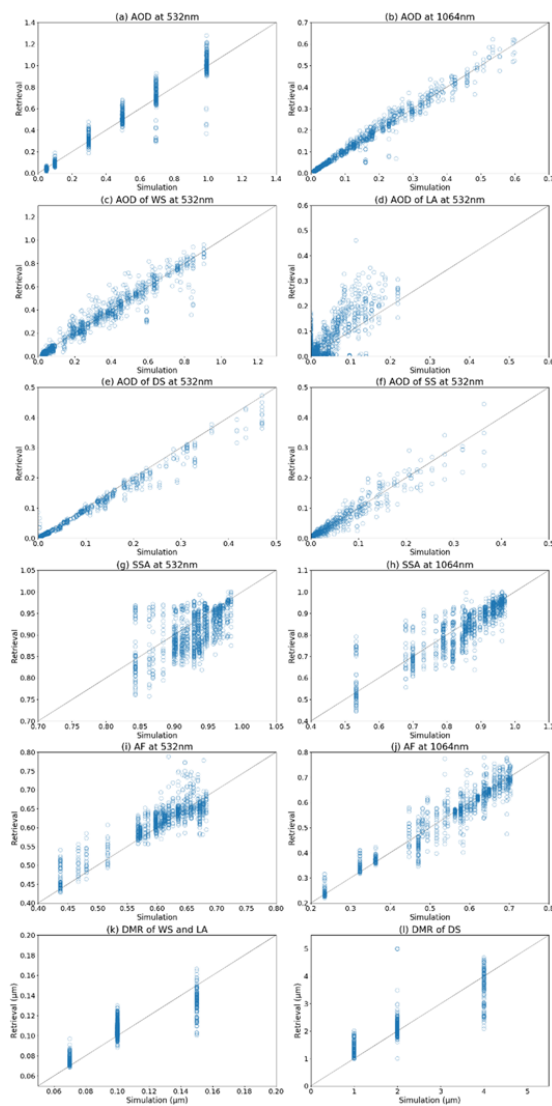
Figure 5. Scatter plots of simulated and retrieved columnar properties: AOD at (a) 532 and (b) 1064 nm; AOD at 532 nm of (c) WS, (d) LA, (e) DS, and (f) SS; SSA at (g) 532 and (h) 1064 nm; AF at (i) 532 and (j) 1064 nm; DMR of (k) fine (WS and LA) and (l) coarse (DS) particles.

965
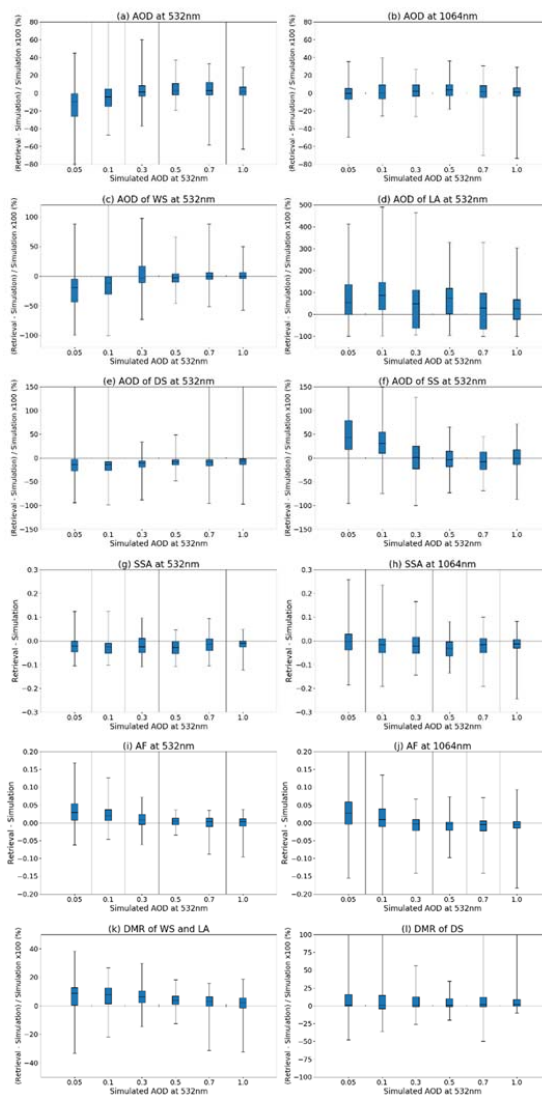
Figure 6. Box and whisker plots for relative or absolute differences of columnar properties between retrievals and simulations. The box extends from the first quartile to the third quartile of the data, with a line at the median. The whiskers extend from the box to 1.5 × inter-quartile range. The column properties are AOD at (a) 532 and (b) 1064 nm; AOD at 532 nm of (c) WS, (d) LA, (e) DS, and (f) SS; SSA at (g) 532 and (h) 1064 nm; AF at (i) 532 and (j) 1064 nm; and DMR of (k) fine (WS and LA) and (l) coarse (DS) particles.
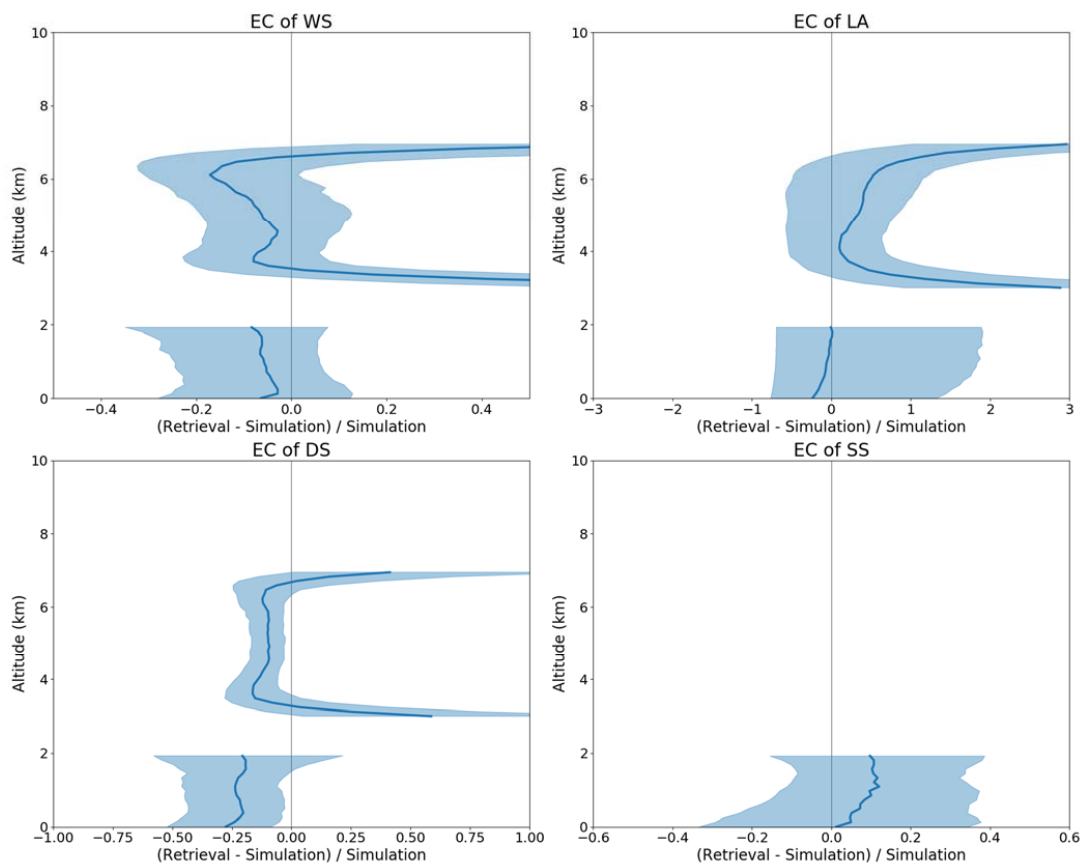
Figure 7. Relative differences of EC at 532 nm for (a) WS, (b) LA, (c) DS, and (d) SS between retrievals and simulations. The shading indicates the areas between the first and third quartiles of the data, and the thick lines indicate median values.
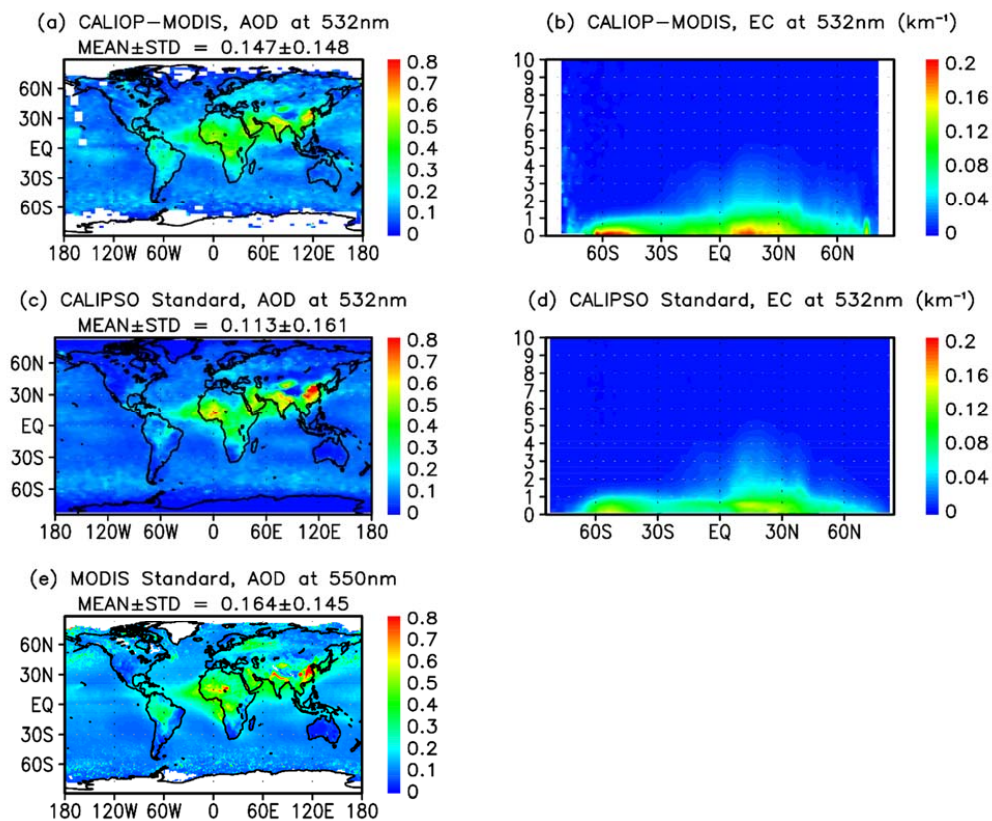
Figure 8. Annual means of AOD and EC in 2010. The left column shows horizontal distributions of AOD, and the right column shows zonal means of EC for the (a, b) CALIOP-MODIS retrieval, (c, d) CALIPSO standard product, and (e) MODIS standard product. At the top of the left panels, MEAN±STD indicates the global mean and its standard deviation.

980
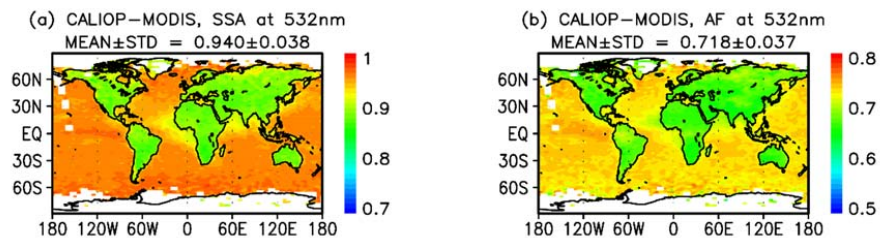
Figure 9. Horizontal distributions of the annual means of (a) SSA and (b) AF in 2010 in the CALIOP-MODIS retrieval. At the top of each panel, MEAN±STD indicates the global mean and its standard deviation.

985
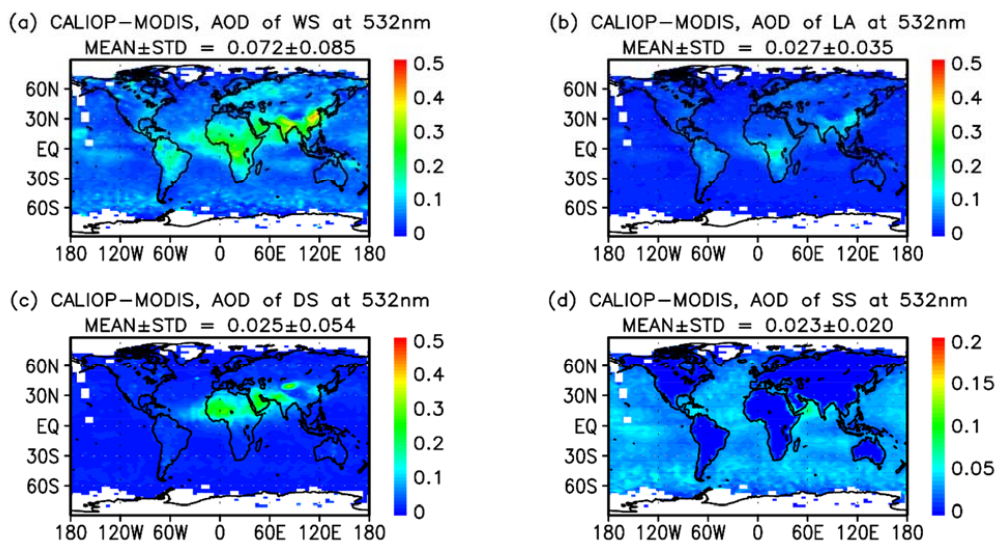
Figure 10. Horizontal distributions of the annual means of the AOD of (a) WS, (b) LA, (c) DS, and (d) SS in 2010 in the CALIOP-MODIS retrieval. At the top of each panel, MEAN±STD indicates the global mean and its standard deviation.

990
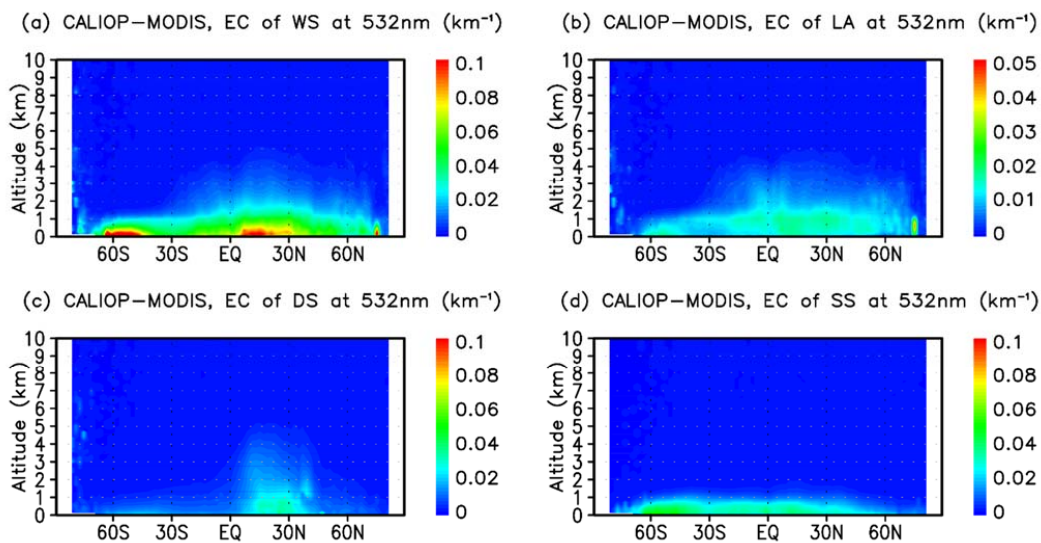
Figure 11. Zonal means of the EC of (a) WS, (b) LA, (c) DS, and (d) SS in 2010 in the CALIOP-MODIS retrieval.
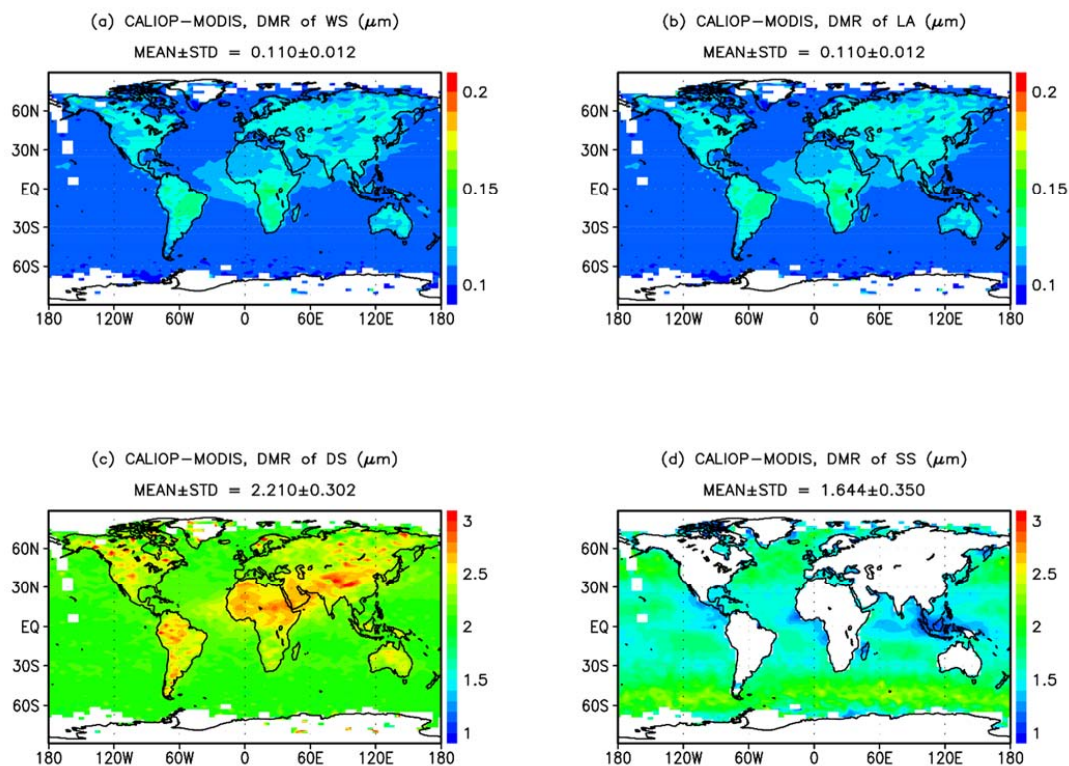
Figure 12. Horizontal distributions of the annual means of the DMR of (a) WS, (b) LA, (c) DS, and (d) SS in 2010 in the CALIOP-MODIS retrieval. At the top of each panel, MEAN±STD indicates the global mean and its standard deviation.
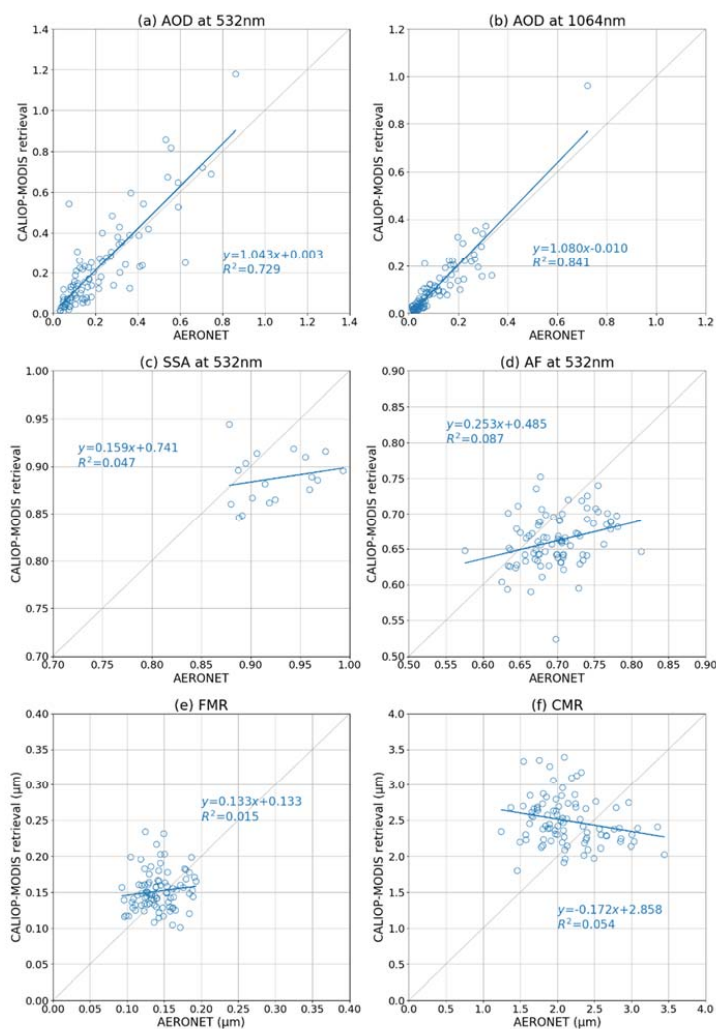
Figure 13. Comparisons of the columnar properties between the AERONET products and CALIOP-MODIS retrieval: AOD at (a) 532 nm and (b) 1064 nm; (c) SSA at 532 nm; (d) AF at 532 nm; (e) fine median radius, and (f) coarse median radius. The linear regression results are shown as equations in the form y = ax + b, and R^2 is the coefficient of determination.

1000
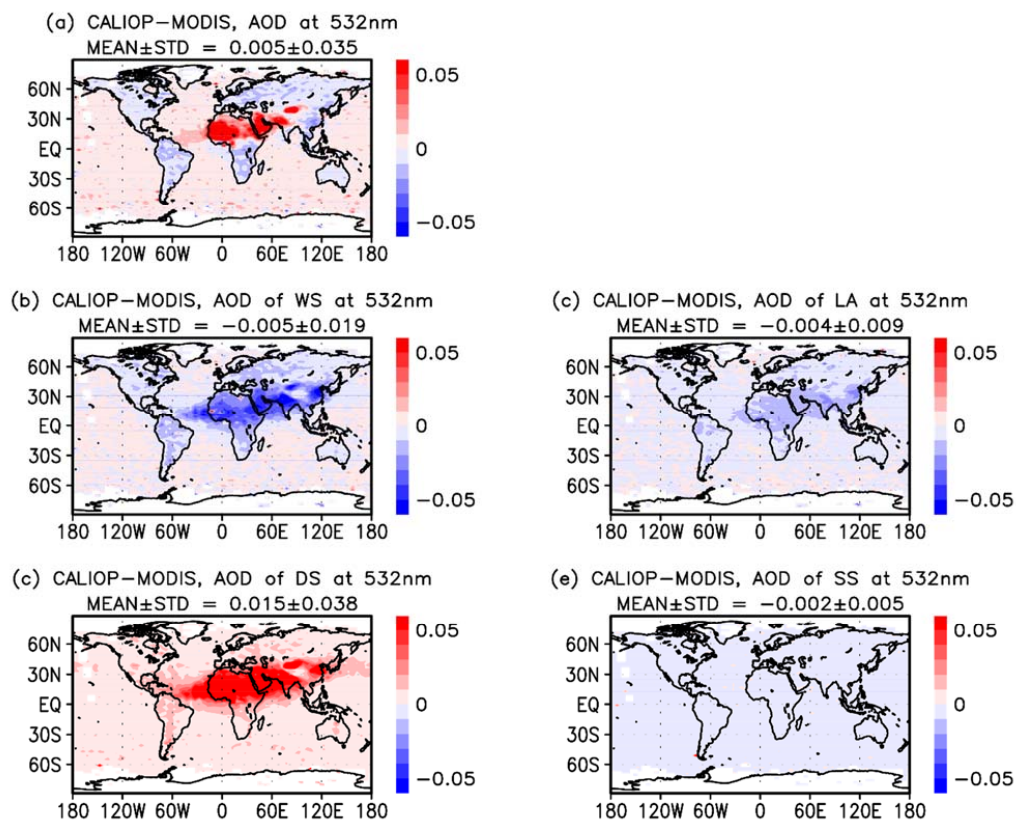
Figure 14. Horizontal distributions of the differences in the retrieved AOD of (a) total aerosols, (b) WS, (c) LA, (d) DS, and (e) SS between the retrievals with spheroid and Voronoi models. At the top of each panel, MEAN±STD indicates the global mean and its standard deviation.

1005
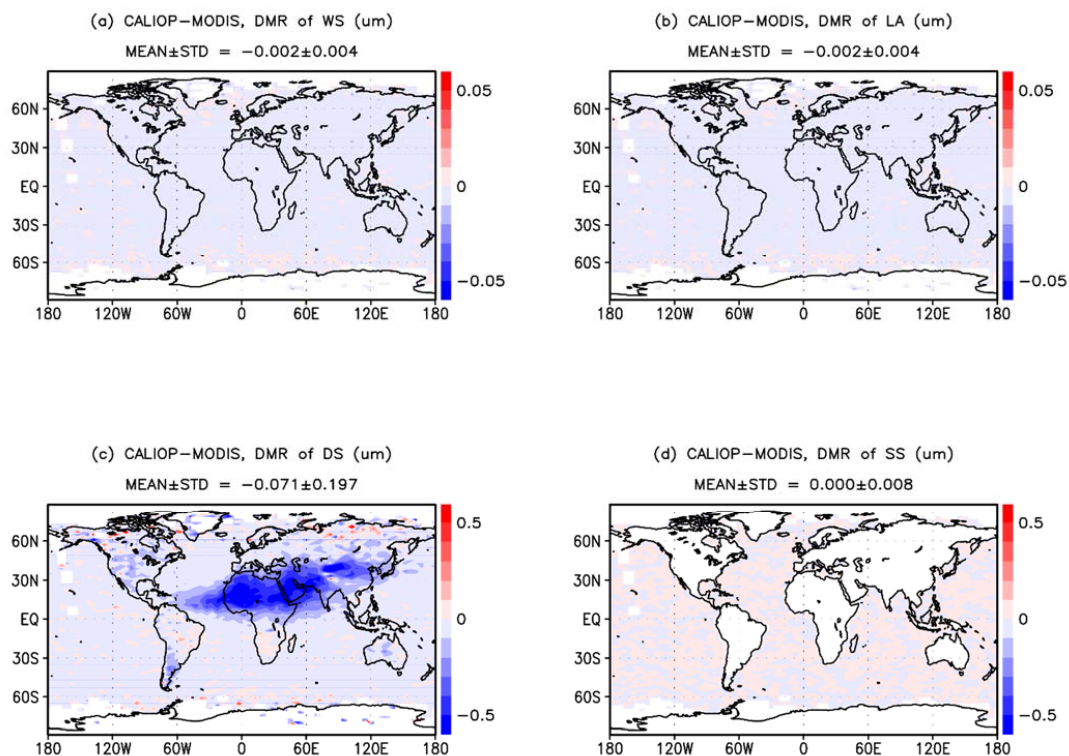
Figure 15. Horizontal distributions of the differences in the retrieved DMR of (a) WS, (b) LA), (c) DS, and (d) SS between the retrievals with spheroid and Voronoi models. At the top of each panel, MEAN±STD indicates the global mean and its standard deviation.

1010
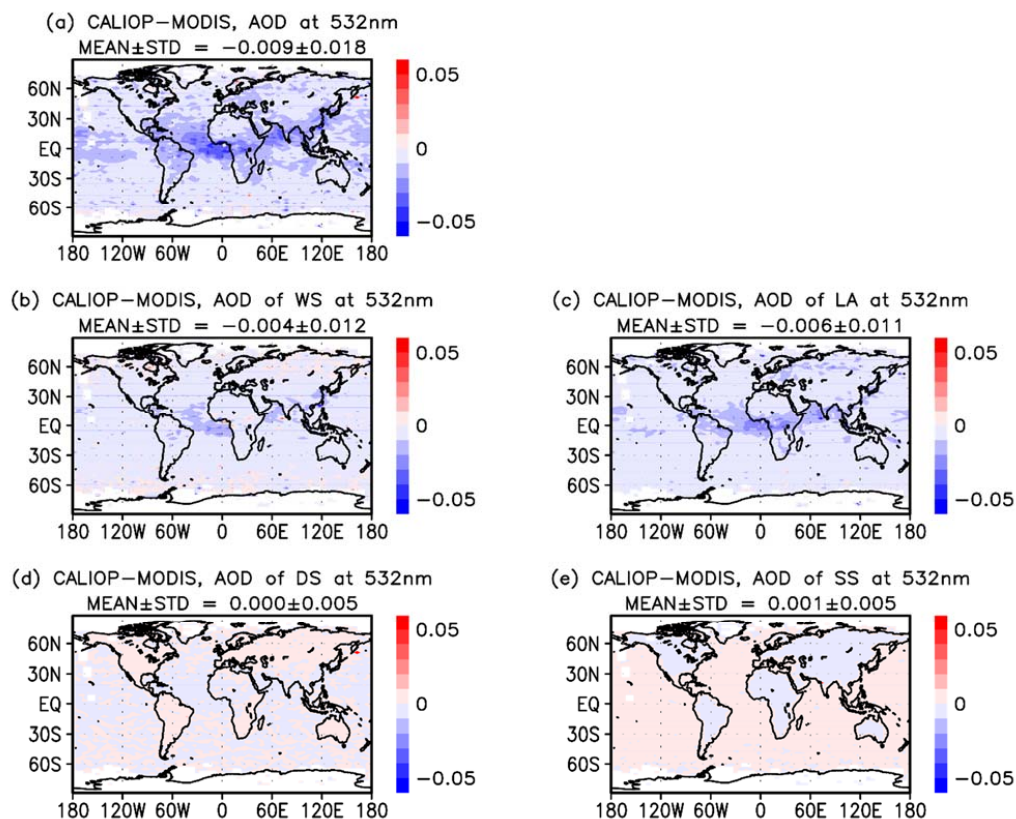
Figure 16. Horizontal distributions of differences in the retrieved AOD of (a) total aerosols, (b) WS, (c) LA, (d) DS, and (e) SS between the retrievals with BC volume fractions of 15 % and 30 %. At the top of each panel, MEAN±STD indicates the global mean and its standard deviation.

1015
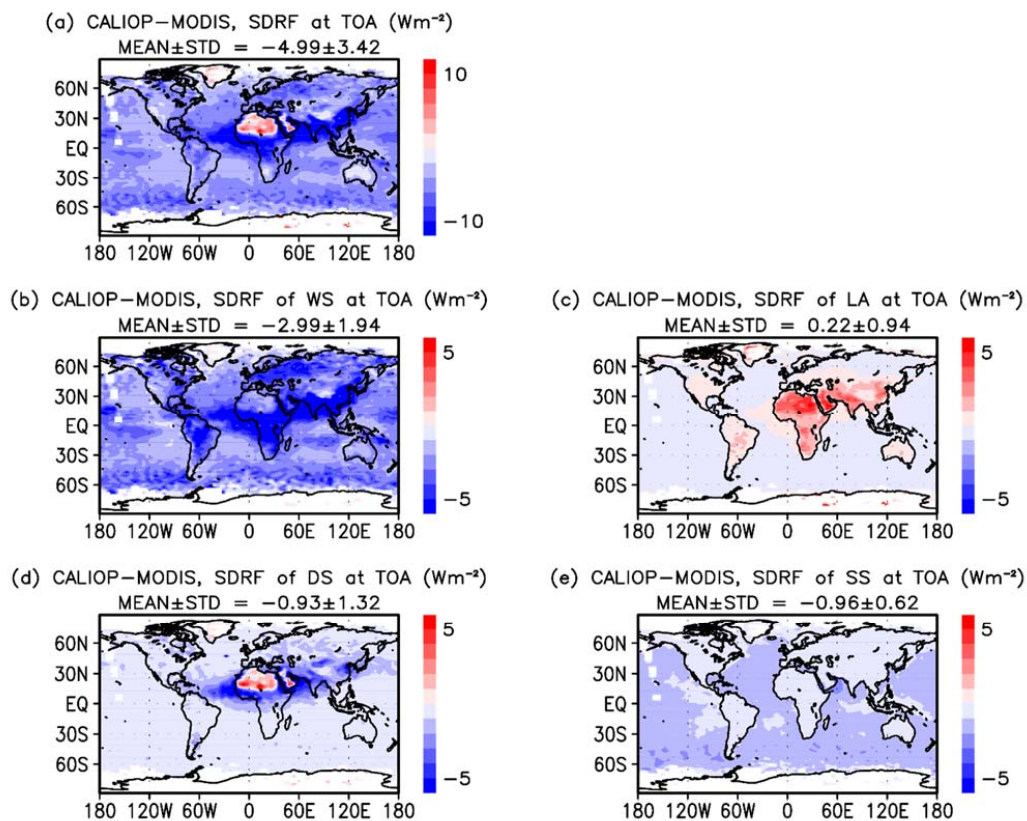
Figure 17. Horizontal distributions of the annual means of the SDRF of (a) total aerosols, (b) WS, (c) LA, (d) DS, and (e) SS (e) at top of the atmosphere (TOA) in 2010. At the top of each panel, MEAN±STD indicates the global mean and its standard deviation.
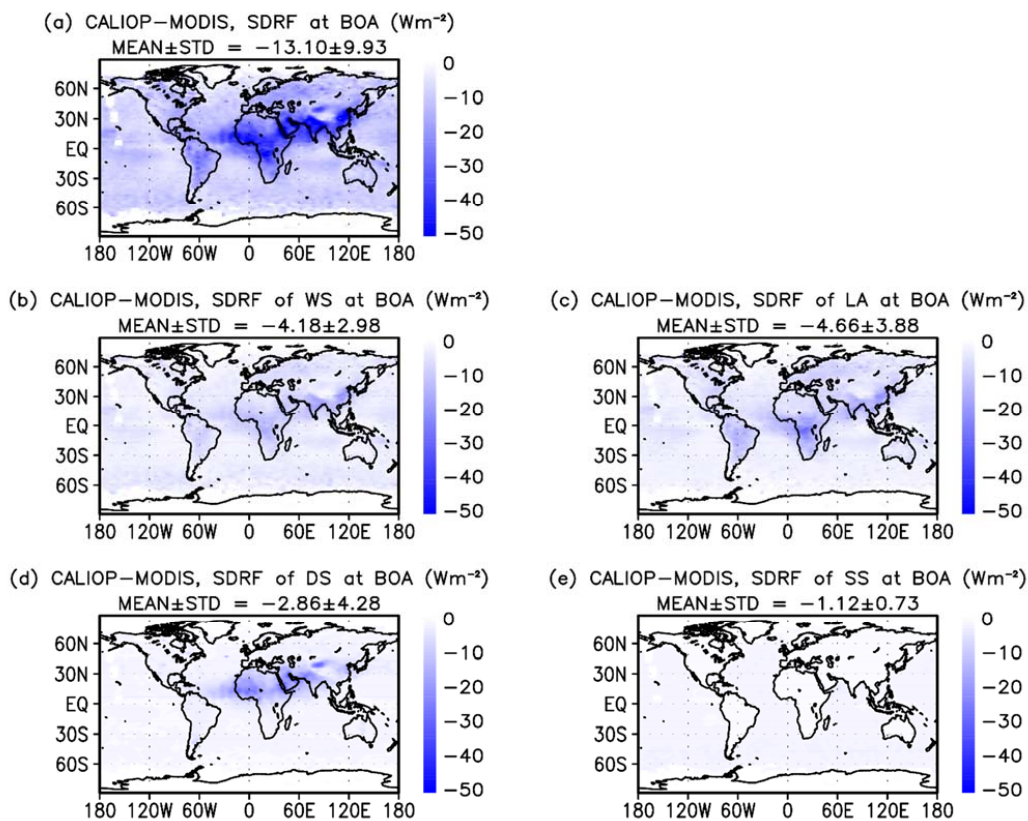
1020

Figure 18. Horizontal distributions of the annual means of the SDRF values of (a) total aerosols, (b) WS, (c) LA, (d) DS, and (e) SS at the bottom of the atmosphere (BOA) in 2010. At the top of each panel, MEAN±STD indicates the global mean and its standard deviation.
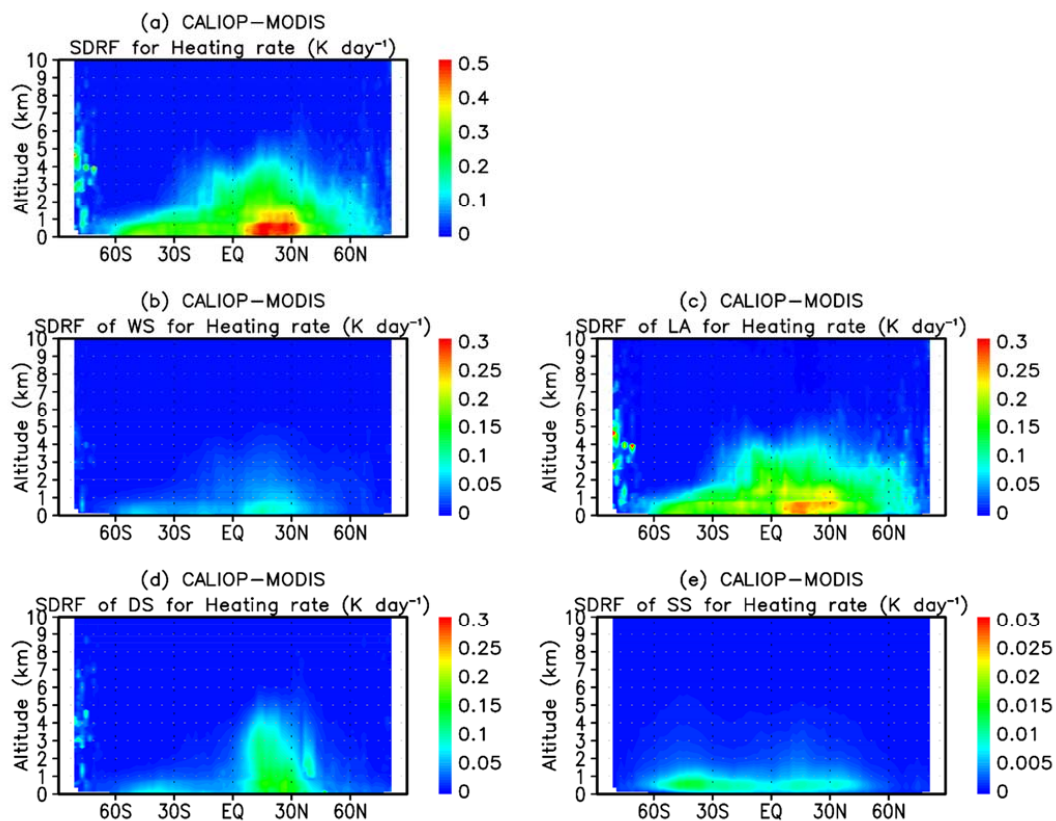
1025

Figure 19. Annual means of impacts of (a) total aerosols, (b) WS, (c) LA, (d) DS, and (e) SS on heating rates in 2010.